Science of the Total Environment 958 (2025) 177984

Contents lists available at ScienceDirect

Science of the Total Environment

journal homepage: www.elsevier.com/locate/scitotenv

From data to insights: Upscaling riverine GHG fluxes in Germany with machine learning

R.M. Mwanake [a,*], E.G. Wangari [a], K. Winkler [a], G.M. Gettel [c,d], K. Butterbach-Bahl [a,b], R. Kiese [a]

[a] Karlsruhe Institute of Technology, Institute for Meteorology and Climate Research, Atmospheric Environmental Research (IMK-IFU), Kreuzeckbahnstrasse 19, Garmisch-Partenkirchen 82467, Germany
[b] Pioneer Center Land-CRAFT, Department of Agroecology, University of Aarhus, Aarhus, Denmark
[c] Aarhus University, Department of Ecoscience, Aquatic Ecology Section, Aarhus, Denmark
[d] IHE Delft Institute for Water Education, Department of Water Resources and Ecosystems, Delft, The Netherlands

HIGHLIGHTS

- Vegetation indices and machine learning models predicted riverine GHG fluxes.
- High spatial variability in modeled fluxes (1.7 to 96.4 kg CO_2-eq m^{-2} yr^{-1}).
- Urban areas and intensive croplands accounted for hotspots of fluvial GHG fluxes.
- German rivers are sources of fluvial GHG fluxes (4.56 (3.01–6.11) Tg CO_2-eq yr^{-1}).

GRAPHICAL ABSTRACT

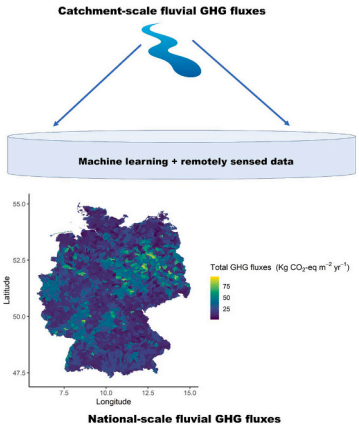

ARTICLE INFO

Editor: Sergi Sabater

Keywords:
Carbon dioxide
Methane
Nitrous oxide
Streams
Vegetation indices
Remote sensing

ABSTRACT

Global fluvial ecosystems are important sources of greenhouse gases (CO_2, CH_4, and N_2O) to the atmosphere, but their estimates are plagued by uncertainties due to unaccounted spatio-temporal variabilities in the fluxes. In this study, we tested the potential of modeling these variabilities using several machine learning models (ML) and three different input datasets (remotely sensed vegetation indices, in-situ water quality, and a combination of both) from 20 headwater catchments in Germany that differ in catchment land use and stream size. We also upscaled fluvial GHG fluxes for Germany using the best ML model and explored the role of catchment land use on the GHG spatial-temporal trends. Model performance depended on the choice of ML model, input data and GHG type. Complex decision-tree-based models better predicted GHG concentrations and fluxes than other ML model types (r^2 = 0.33 to 0.72). Our upscaled fluxes from catchment scale remotely sensed vegetation indices showed that total annual riverine CO_2 equivalent fluxes from 2934 catchments in Germany ranged from 1.7 to 96.4 kg m^{-2} yr^{-1} (mean ± SE: 23.2 ± 0.001). The highest fluxes came from urban and intensively cropped catchments,

* Corresponding author.
E-mail address: ricky.mwanake2@kit.edu (R.M. Mwanake).

https://doi.org/10.1016/j.scitotenv.2024.177984
Received 17 September 2024; Received in revised form 14 November 2024; Accepted 5 December 2024
Available online 14 December 2024

while lower fluxes came from extensively cropped, forestry, and pasture-dominated catchments. Our study demonstrates that spatially and temporally resolved catchment vegetation indices from remotely sensed data in conjunction with machine learning models can be applied to upscale all three GHG concentrations and fluxes from diverse catchments, revealing important spatio-temporal trends associated with catchment land use.

1. Introduction

Streams and rivers are important sources of greenhouse gases (GHGs: CO_2, CH_4, and N_2O) to the atmosphere, contributing approximately 10 %, or 5.3 Pg CO_2-eq. yr^{-1}, of the global annual CO_2-equivalent fluxes from all sectors, including land use changes, energy, and industry (Jones et al., 2023; Lauerwald et al., 2023). Of these fluxes, headwater streams are considered to be hotspots compared to large rivers, accounting for over 70 % of total riverine fluxes (Li et al., 2021). However, despite their significant contributions to global GHG fluxes, the wide range (~5 Pg CO_2-eq. yr^{-1}) in riverine GHG flux estimates indicates significant uncertainties. These uncertainties are mostly related to the lack of globally distributed field-based measurements, short temporal coverage, and upscaling uncertainties when point measurements are upscaled to basin-wide or even global scales (e.g., Lauerwald et al., 2023).

Most empirical datasets of riverine GHG concentrations and fluxes have been developed using synoptic sampling approaches (e.g., Aho and Raymond, 2019; Mwanake et al., 2019, 2023a). While recent advances in high-precision GHG sensors can help to increase the temporal coverage of riverine GHG concentrations to sub-daily scales (e.g., Piatka et al., 2024), sensors that cover all three GHGs remain expensive, which limits the spatial coverage of such measurements (Dalvai Ragnoli and Singer, 2024). Moreover, although efforts have been made to develop cheaper sensors (Bastviken et al., 2015, 2020; Leith et al., 2015), these sensors are mostly limited to CO_2 and CH_4 and additionally require technical expertise to set up and operate (e.g., Dalvai Ragnoli and Singer, 2024).

Statistical modeling approaches driven by various environmental drivers of fluvial GHG concentrations and fluxes have shown promise in overcoming the spatio-temporal limitations of direct field measurements (Panique-Casso et al., 2024). These environmental drivers include in situ water quality parameters such as organic matter (OM), nutrients, electron acceptors, and temperature, which are known to influence in situ GHG production and consumption processes either as substrates or catalysts (Quick et al., 2019; Raymond et al., 2013; Stanley et al., 2016), and broader-scale factors such as stream size, catchment land use, soil conditions, topography, and discharge, which are known to determine the magnitude of the in situ water quality parameters, gas exchange rates with the atmosphere, and the external sources of the GHGs (Hotchkiss et al., 2015; Mwanake et al., 2022; Rocher-Ros et al., 2023). Despite the promise of such modeling approaches, the spatio-temporal coverage of similar modeling efforts have been hampered by the sensor and human capital costs associated with the continuous quantification of discharge and water quality parameters. This calls for alternative, cost-effective, and efficient ways to spatially and temporally upscale fluvial GHG concentrations and fluxes with limited inputs from field measurements (Panique-Casso et al., 2024).

Recent advances in readily available remotely sensed datasets and machine learning technologies may provide an alternative way to model riverine GHG concentrations and fluxes in space and time using the available field-based datasets. Remotely sensed datasets derived from satellite images provide rich spatial and temporal data that can reflect catchment characteristics, potentially acting as predictors for riverine GHG concentrations (e.g., Liu et al., 2022; Martinsen et al., 2020; Rocher-Ros et al., 2023; Xiong et al., 2024). For example, vegetation indices describing vegetation quantity and its water content derived from sentinel 2 satellite images have recently been shown to predict the spatio-temporal trends in soil GHG fluxes (Wangari et al., 2023), which may also reflect riverine GHG fluxes through soil to river hydrological transfer of nutrients, OM and dissolved GHG concentrations (e.g., Mwanake et al., 2023a, 2023b). When combined with machine learning (ML) algorithms, which are computationally less demanding and require less parameterization compared to traditional process-based models (Panique-Casso et al., 2024), these datasets can effectively model the spatiotemporal trends in fluvial GHG concentrations and fluxes.

Although such an approach has been applied to quantify GHG concentrations or fluxes in several aquatic ecosystems, these studies so far have primarily focused on lentic ecosystems such as lakes and oceans (e.g., Bai et al., 2015; Olsen et al., 2004; Parard et al., 2015; Qi et al., 2023; Valerio et al., 2021). However, only a handful of studies have been conducted in lotic ecosystems, and these have mainly focused on global-scale trends and drivers (Liu et al., 2022; Marzadri et al., 2021; Rocher-Ros et al., 2023), potentially overlooking local-scale dynamics. Such local scale heterogeneities may be related to differences in upstream land use, topography, and hydro-climatic conditions. For example, excess nutrient and labile OM supplies in urban and agricultural-dominated catchments may result in elevated riverine GHG concentrations due to favored instream GHG production or external dissolved GHG sources (e.g., Begum et al., 2021; Borges et al., 2018; Upadhyay et al., 2023). On the other hand, hydrological and topographical conditions may influence gas exchange rates between the water column and the atmosphere (e.g., Raymond et al., 2012).

This study aimed to determine the potential of machine learning approaches to upscale CO_2, N_2O, and CH_4 concentrations and fluxes from diverse catchments in Germany, covering a catchment land use gradient from extensive natural forests to intensive agricultural and urban areas. Input datasets for the model calibration and validation included temporally resolved remotely sensed vegetation indices, in situ water quality data, and a combination of both datasets from 20 headwater catchments in Germany covering land use, stream size, topographic, and climatic gradients. Our specific objectives were to a) determine the potential of vegetation indices derived from remotely sensed Sentinel-2 data in modeling riverine GHG concentrations and fluxes, b) compare the predictive performance of the remotely sensed data with models built with water quality parameters and a combination of both, and to c) upscale GHG concentrations and fluxes for all of Germany and assess the role of land use in explaining the spatio-temporal trends. By potentially describing nutrient and OM matter conditions within catchments, we hypothesized that remotely sensed data would be able to model riverine GHG concentrations and fluxes, allowing upscaling of GHG contributions from multiple streams with limited input field data. We also hypothesized that heterogeneities in the upscaled riverine GHG fluxes would relate to catchment land use intensities. For instance, higher values will be recorded for catchments dominated by intensive agriculture and urban areas due to additional nutrient and labile OM supplies than for catchments covered by natural ecosystems.

2. Materials and methods

2.1. Site-scale data acquisition

For this study, we used a previously published dataset from 20 stream sites in three catchments in Germany, i.e., the Loisach, Schwingbach, and Neckar rivers, collected between 2020 and 2022 at biweekly-triweekly intervals during the day (Table 1; Fig. A1; Mwanake, 2023). The catchments were diverse in terms of their coverage of different land uses (forests, croplands, urban areas, grasslands, and

wetlands), stream sizes (stream orders 1–6; Strahler classification), and locations, i.e., from the south to the central part of Germany, with different weather patterns and topographical conditions (Table 1; Fig. A1). The dataset also included key water quality variables such as dissolved oxygen (DO), water temperature, electrical conductivity, dissolved organic carbon (DOC), nitrate (NO_3-N), and ammonium (NH_4-N), as well as GHG (CO_2, CH_4, and N_2O) concentrations and fluxes (units of mass m^{-2} of stream surface day^{-1}). Uniform quantitative sampling and analytical methodologies were applied at all 20 catchments. In brief, water temperature (°C), electrical conductivity (μS cm^{-1}), and dissolved oxygen (DO) (mg L^{-1}) were quantified in situ using the Pro DSS multiprobe (YSI Inc., USA). Water samples for nutrient and dissolved organic carbon (DOC) analyses were collected and filtered on-site through polyethersulfone (PES) filters (0.45 μm pore size, pre-leached with 60 ml of miliq water). In the laboratory, these samples were directly analyzed for NO_3-N and NH_4-N concentrations using colorimetric methods, and the absorbance of the samples was measured using a microplate spectrophotometer (Model: Epoch, BioTek Inc., USA). The DOC concentrations were measured as non-purgeable organic carbon (NPOC) using a TOC/TN analyzer (Analytica-Jena; multi N/C 3100, Germany).

GHG concentrations in the stream water were sampled in situ using the headspace equilibration technique and analyzed on a gas chromatograph (SRI 8610C, Germany). The final dissolved GHG concentrations in the water were then calculated based on Henry's solubility constants. Daily diffusive fluxes (F) (mass m^{-2} d^{-1}) of the GHGs were estimated using Fick's Law of gas diffusion, where the F is the product of the gas exchange velocity (k) (m d^{-1}) and the difference between the stream water (C_{aq}) (mass m^{-3}) and the ambient atmospheric gas concentration in water assuming equilibrium with the atmosphere (C_{sat}) (mass m^{-3}) (Eq. (1)). The temperature-specific gas transfer velocities (k) for each of the gases were calculated from normalized gas transfer velocities (k_{600}) (m d^{-1}) modeled from measured stream velocity (m s^{-1}) and slope (m m^{-1}) values using eq. 4 from Raymond et al., 2012. A detailed description of the study areas, analytical methods, and GHG flux calculations can be found in the respective publication (Mwanake et al., 2023a).

$$F = k\left(C_{aq} - C_{sat}\right) \tag{1}$$

2.2. Remotely sensed vegetation data acquisition

Upstream catchments for each of the 20 sites were delineated in QGIS (Quantum Geographic Information System) using a 30 m spatial resolution Digital Elevation Model (DEM) (EU-DEM v1.1). Subsequently, vegetation characteristics for each catchment and close to each sampling date (±10 days) were derived from 6 spectral bands (red, blue, green, near-infrared, shortwave 1 and 2) of Sentinel 2 raster images with low cloud cover (<5 %) and a 10 m spatial resolution. These Sentinel 2 raster images were automatically acquired using the "Openeo" package (R version 4.3.2.) from the European Space Agency (ESA) Copernicus Data Space Ecosystem (https://openeo.dataspace.copernicus.eu/openeo/1.2; last accessed: April 4, 2024) and combined to form a raster brick. In cases where more than one raster brick image with all six bands meeting the cloud cover threshold was available for individual catchments for each sampling date, the median of these images was calculated and used to represent the conditions of those catchments. Vegetation cover was estimated from the final Sentinel 2 raster brick images of all 20 sites and sampling dates using the simple ratio index (SR), normalized difference vegetation index (NDVI), and green normalized difference vegetation index (GNDVI), calculated from the near-infrared (NIR), red, and green bands (Bannari et al., 1995; Gitelson and Merzlyak, 1998; Eqs. (2), (3), and (4)). Vegetation water content was also estimated using the normalized difference moisture index (NDMI), normalized difference infrared Index (NDII), moisture stress index (MSI), and normalized difference water index (NDWI), calculated from the near-infrared (NIR) and shortwave infrared (SWIR1, 2) bands (Wangari et al., 2023; Gao, 1996; Eqs. (5), (6), (7), and (8)). Catchment means were calculated to convert the gridded vegetation indices into numerical values aggregated for each site and sampling time.

$$\mathrm{SR} = \frac{\mathrm{NIR}}{\mathrm{red}} \tag{2}$$

$$\mathrm{GNDVI} = \frac{\mathrm{NIR} - \mathrm{green}}{\mathrm{NIR} + \mathrm{green}} \tag{3}$$

$$\mathrm{NDVI} = \frac{\mathrm{NIR} - \mathrm{red}}{\mathrm{NIR} + \mathrm{red}} \tag{4}$$

$$\mathrm{NDMI} = \frac{\mathrm{NIR} - \mathrm{SWIR1}}{\mathrm{NIR} + \mathrm{SWIR1}} \tag{5}$$

Table 1
Description of sampling sites located in the Schwingbach, Loisach, and Neckar catchments (Fig. A1). The land use (%) was calculated for the site-specific upstream catchments based on the Corine Land Cover 2018 survey of Europe.

Main catchment	Stream order	Catchment area (km^2)	Coordinates		Elevation at sampling point	Sub-catchment Landuse/landcover (%)					Main sub-catchment landuse class
			Latitude	Longitude		Forest	Wetland	Grassland	Cropland	Urban	
Loisach	1	0.04	47.5694	11.1554	651	40	60	0	0	0	Wetland
Loisach	2	0.10	47.5689	11.1556	645	22	78	0	0	0	Wetland
Loisach	1	0.11	47.544	11.1193	660	0	0	100	0	0	Grassland
Loisach	1	0.13	47.5399	11.1105	663	19	0	81	0	0	Grassland
Loisach	1	0.40	47.467	11.0537	750	86	0	14	0	0	Forest
Loisach	2	0.75	47.4691	11.0394	756	99	0	0	0	1	Forest
Loisach	2	1.02	47.5858	11.1429	719	100	0	0	0	0	Forest
Schwingbach	1	0.41	50.5051	8.6127	297	96	0	0	4	0	Forest
Schwingbach	1	0.60	50.4695	8.6179	187	0	0	0	100	0	Cropland
Schwingbach	2	0.62	50.4811	8.5407	241	98	0	2	0	0	Forest
Schwingbach	1	0.67	50.4756	8.5472	334	86	0	0	14	0	Forest
Schwingbach	2	2.20	50.4922	8.5971	260	47	0	0	53	0	Cropland
Schwingbach	2	2.20	50.5032	8.5553	272	65	0	0	35	0	Forest
Schwingbach	1	3.55	50.4669	8.5792	207	14	0	0	84	2	Cropland
Schwingbach	3	23.37	50.505	8.6148	183	37	0	6	48	9	Cropland+Urban
Schwingbach	3	53.45	50.5166	8.5992	189	44	0	4	45	7	Cropland+Urban
Neckar	5	116.23	48.5588	9.0591	367	97	0	0	3	0	Forest
Neckar	5	261.57	48.5649	8.8986	379	11	0	1	84	4	Cropland+Urban
Neckar	6	304.41	48.5271	8.9615	348	14	0	2	77	8	Cropland+Urban
Neckar	6	513.32	48.4796	9.0634	348	74	0	10	11	4	Forest+Urban

$$NDII = \frac{NIR - SWIR2}{NIR + SWIR2} \quad (6)$$

$$MSI = \frac{SWIR1}{NIR} \quad (7)$$

$$NDWI = \frac{green - NIR}{green + NIR} \quad (8)$$

2.3. Modeling of riverine GHG concentrations and fluxes

A total of nine machine-learning algorithms were tested for modeling riverine GHG concentrations and fluxes using three datasets: remotely sensed vegetation indices (RS), in-situ water-quality data (WQ), and a combination of both (WQRS) (see Table 2; Fig. 1). These algorithms included a variety of model structures, including decision trees (rf, gbm, xgbLinear, and xgbTree), support vectors (svmRadial), simple neural networks (nnet), k-means clustering (knn), elastic net multiple regression models (glmnet), and a combination of principal component analysis and multiple regression (pls).

For the prediction of riverine GHG concentrations and fluxes, we used the "CARET" (Classification And REgression Training) package in R. During model construction, the input datasets were divided into training (80 %) and test (20 %) sets by randomly sampling the entire dataset without regard to specific sites or sampling dates (Fig. 1). In addition to this hold-out approach for model validation, we implemented a 5-fold cross-validation scheme on the training dataset using the "trainControl" function to internally validate our models and mitigate overfitting (Berrar et al., 2019). Using the "set. seed" function, we specified a value (142) to ensure the reproducibility of the model results across multiple runs. For decision tree-based models, we automatically tuned the most critical hyperparameter (mtry), which represents the number of variables in each prediction tree node within the CARET package. This tuning process involved analyzing the sensitivity of the mtry value to changes in the mean absolute error (MAE) over five iterations and selecting the mtry value that yielded the lowest MAE. To explore whether the models' predictions could be improved for high values of GHG concentrations and fluxes, we applied a natural log transformation to the GHG concentrations and fluxes, which were not normally distributed and skewed towards relatively low values.

2.4. Assessment of model performance

We compared the performance of nine machine learning models by assessing the Mean Absolute Error (MAE) and the coefficient of determination (r^2) (Fig. 1). The MAE was chosen over the RMSE because it is easier to interpret (represents the average absolute differences between observed and predicted values), is less sensitive to outliers, and better represents data sets that are not normally distributed (Willmott and Matsuura, 2005). The best models for each predictor dataset (RS, WQ, WQRS) were selected based on those with the lowest MAE and the highest r^2. Next, the predictor variables in the best models were ranked according to their importance using the "varImp" function in "CARET". The top three predictors for each model that accounted for >60 % of the variance were selected for display in the summary table. To further evaluate the performance of the best models, we performed a regression analysis of predicted versus observed GHG concentrations and fluxes using the test dataset (20 %) that was not used in model building (Fig. 1).

Table 2
Summary of the nine machine learning models tested for predicting GHG concentrations and fluxes. The models' abbreviations are included in the brackets.

Machine learning model	Model structure
Random Forest (rf)	Decision trees
Gradient Boosting Machine (gbm)	Decision trees
Support Vector Machine with Radial Basis Function Kernel (svmRadial)	Support vector
Generalized Linear Model with Elastic Net Regularization (glmnet)	Elastic-net multiple regression models
Feedforward Neural Network (nnet)	Neural-network
eXtreme Gradient Boosting with Linear Booster (xgbLinear)	Decision trees
eXtreme Gradient Boosting with Tree Booster (xgbTree)	Decision trees
k-Nearest Neighbors (knn)	k-means clustering
Partial Least Squares Regression (pls)	Priciple componet analysis and multiple regression models

2.5. Upscaling of annual (2020) riverine GHG concentrations and fluxes for Germany

To explore the applicability of ML models with remotely sensed data to spatially upscale riverine GHG concentrations and fluxes from multiple catchments with contrasting hydrological and landscape characteristics, we used all of Germany as the boundary condition for our modeling experiment (Fig. 1). The rationale for this upscaling experiment was guided by the fact that our training data also covered different parts of Germany (south to central) and was characterized by small to mid-size streams with contrasting upstream land uses and elevations, representing diverse streams and rivers for the upscaling exercise. First, we obtained catchment boundaries for Germany from the global hydrobasin dataset (Level 12; retrieved July 1, 2024: https://www.hydrosheds.org/products/hydrobasins). This dataset consisted of 2934 nested catchments with upstream sub-basin areas ranging from 0.1 to 489 km^2, representing stream orders 0 to 6, similar to our training dataset (Table 1; Fig. A1). Second, we obtained cloudless annual (2020) median Sentinel-2 raster images for Germany from the European Space Agency online database, which served as the input remotely sensed data for our ML models (retrieved July 1, 2024: https://viewer.esa-worldcover.org/worldcover/). The raster images consisted of two raster bricks representing four raster bands in the red, blue, green, and near-infrared regions of the spectrum with 10 m spatial resolutions and three raster bands in the short-wave infrared region of the spectrum with 20 m spatial resolutions.

Several preprocessing steps were performed on the raw Sentinel-2 raster images in R before modeling. First, the two raster images were statistically downscaled (bilinear) from their original resolutions to a resolution of 1 km by 1 km, which is close to the smallest upstream area in the resulting catchment dataset and also helps to reduce the computational time for the modeling (function "rast" in the "terra" package in R). Second, seven vegetation indices similar to those in the training dataset (NDVI, GNDVI, SR, NDMI, MSI, NDII, NDWI) were computed from the two rasters, and the final product containing all 7 indices was combined into one raster brick ("rast" function in the "terra" package in R). Finally, catchment mean values for each of the seven vegetation indices were computed and combined into a new raster brick to form the primary input dataset for the model.

After these preprocessing steps, the annual median riverine CO_2, CH_4, and N_2O concentrations and diffusive fluxes (m^{-2} of stream surface area) for each catchment were then predicted based on the best model described in the previous subsection and the input vegetation index grid, using the "predict" function in the CARET package in R (Fig. 1). Since these modeled concentrations and fluxes at the catchment scale represented annual median values due to the temporal coverage of the input Sentinel-2 raster imagery, the fluxes were finally upscaled to the annual scale by multiplying by 365 days of the year, assuming that the median value also accounted for the seasonality in each of the catchments. An additional validation step apart from the 20 % test data was then performed on the final model results (Fig. 1). This was done by comparing the available GHG concentrations and fluxes measured from previous studies in Germany from the GRiMeDB database (Fig. A1; Table A5; Stanley et al., 2023) and the final predicted median values from the German riverine GHG flux map for 2020 (Fig. 1).

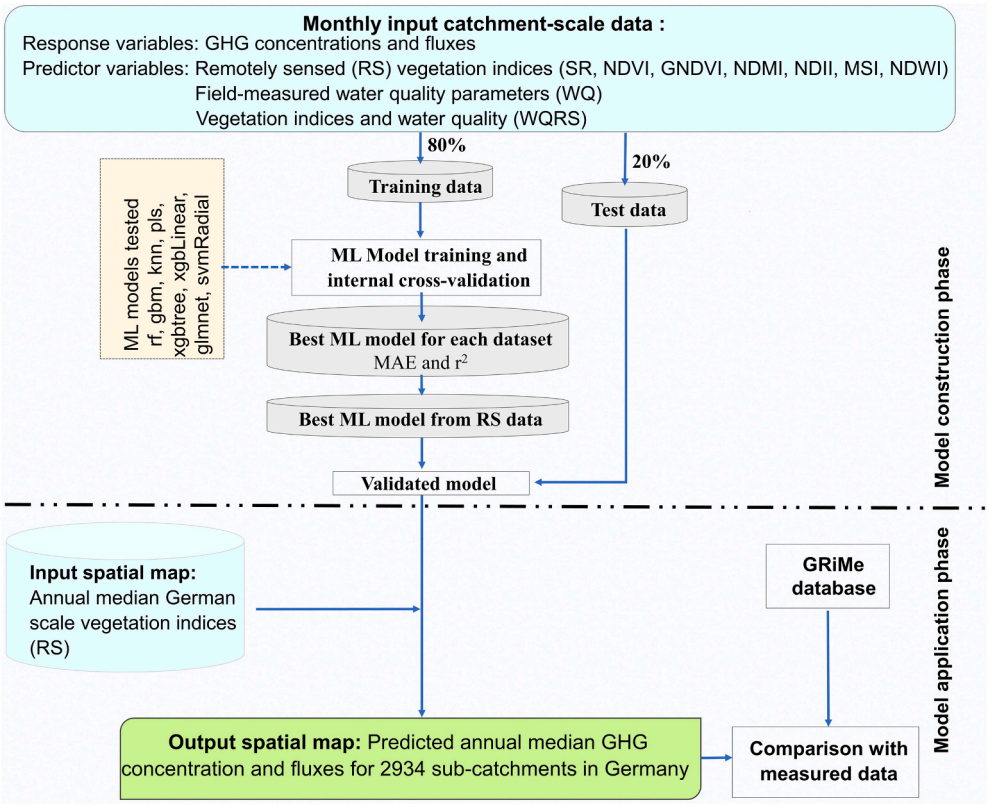

Fig. 1. Workflow summary of the modeling process from calibration and validation with three different input datasets (model construction phase) to the final upscaling of the catchment scale GHG concentrations and fluxes for the entire Germany (model application phase).

We also calculated the aerially resolved riverine GHG fluxes for Germany by summing up the annual fluxes for the individual catchments. These areal fluxes were calculated by multiplying the catchment scale annual median diffusive GHG fluxes (units of mass m^{-2} yr^{-1}) and the river surface areas (m^2). Catchment-specific river surface areas were computed by multiplying the stream length and the bankfull-widths modeled from long-term discharge using a power-law relationship (See eq. 10 of Xu et al., 2020). Both the stream lengths and the long-term discharge for each catchment were derived from the HydroRIVERS database (retrieved on 11/11/2024; https://www.hydrosheds.org/products/hydrorivers). The total riverine GHG fluxes for catchments in Germany were also computed as CO_2-equivalent fluxes using the 100-year global warming potentials, i.e., 28 for CH_4 and 273 for N_2O.

2.6. Effect of land use intensity on modeled GHG concentrations and fluxes

To determine how land use intensity affects the spatio-temporal heterogeneities of riverine GHG concentrations and fluxes, we used a detailed land use map for Germany that differentiates land uses and also examines the intensity of management within them, e.g., intensively managed croplands vs. extensively managed croplands (Table A2; Table A3). The map is a harmonized product generated from multiple remotely sensed land cover data at the German and European scales (Table A2). To create this synthesis map, the fractional coverage of the land use classes from each input product was first resampled and reprojected onto a standard 1 km spatial resolution. A rule-based classification was applied for each target land use class (see detailed land use classes in Table A3). The average land use fraction from the input data was used as a probability map for individual land use classes. Probability maps for the different land use classes were stacked, and each grid cell was assigned the land use class with the highest probability value. In a second step, the land use map was iteratively calibrated against national land use statistics for 2020 (Table A4). The map was repeatedly reclassified using the probability maps so that national land use areas approximated the official area statistics as closely as possible. The final land use map covers Germany, has a spatial resolution of 1 km and contains 31 land use classes with different land use intensity levels for 2020. Since the study focused more on intensity levels related to urbanization and cropland due to their impact on nutrient-driven elevated GHG concentrations (e.g., Wang et al., 2024; Xu et al., 2024), the 31 land use classes were aggregated into 7 different land use classes, which mainly reflected urban areas and cropland land use intensity (see aggregated land use class in Table A3). In brief, the 7 land use classes were intensive croplands (high fertilization: ca. 250 kg N/ha; potentially irrigated), extensive croplands (low fertilization: ca. 100 kg N/ha; rainfed), urban areas, pastures (intensive-extensive), forestry (intensive-extensive), solar and others (sparsely or unmanaged land, mining areas, wetlands, shrubs, barren land, rocks and ice). Land use percentages for each of the 2934 catchments were calculated from the land use map containing these 7 distinct land use classes. The dominant land class for each catchment (>50 % of a single land use class) was then determined. When none of the 7 classes dominated the catchments, these catchments were classified as those with mixed land use. The median GHG fluxes for each dominant land use class were compared from the highest to the lowest to assess the effect of land use and land use intensity on riverine GHG fluxes. Pairwise mean comparisons using the Wilcoxon test were then conducted to determine significant differences in the riverine fluxes across the dominant land use classes.

3. Results

3.1. Comparison of the ML models

Measured GHG concentrations for the 20 catchments ranged from 219.96 to 3861 μg L^{-1} (mean; 1135.0) for CO_2-C concentrations,

0.12–51.6 μg L^{-1} (2.82) for CH_4-C concentrations, and 19.6–4424 ng L^{-1} (830.9) for N_2O-N concentrations. As for the fluxes, they ranged from −0.73–174.38 g m^{-2} d^{-1} (18.4) for CO_2-C fluxes, 0–307.8 mg m^{-2} d^{-1} (31.6) for CH_4-C fluxes, and −18.5–162.8 mg m^{-2} d^{-1} (12.1) for N_2O-N fluxes (Table A1). Model performance, as indicated by both the coefficient of determination (r^2) and the MAE, varied based on the chosen machine learning algorithm, the input dataset, and the type of greenhouse gas (GHG) (Table 3; Figs. A2, A3, A4). Decision tree-based models generally performed better than other model structures, accounting for all of the best-performing models, with coefficients of determination ranging from 0.33 to 0.72 (Table 3). Among these, gradient-boosting models (gbm, xgbTree, and xgbLinear) typically outperformed random forest models, regardless of the input dataset (Table 3). For example, CO_2 concentrations and fluxes were most accurately predicted by these models, with average model uncertainties across the three input datasets (% of MAE relative to the measured mean values) of ±4.9 % for CO_2 concentrations and ± 6.7 % for CO_2 fluxes (Table 3). Notably, NDWI emerged as the most influential predictor for CO_2 concentrations and fluxes in the remote sensing dataset, while water temperature was the top predictor in the water quality dataset (Table 3). Similar to CO_2, CH_4 concentrations and fluxes were best predicted by the gradient boosting models, with average model uncertainties across the three input datasets of ±76.1 % for CH_4 concentrations and ±17.0 % for CH_4 fluxes (Table 3). NDII and NDWI stood out as the primary predictors for CH_4 concentrations and fluxes in the remote sensing dataset, while water temperature and NO_3 demonstrated more substantial predictive power for CH_4 dynamics in the water quality dataset (Table 3). In contrast to CO_2 and CH_4, N_2O concentrations and fluxes were better predicted by the random forest models, with average model uncertainties across the three input datasets of ±6.3 % for N_2O concentrations and ±11.6 % for N_2O fluxes (Table 3). Vegetation quality indices such as NDVI and GNDVI emerged as strong predictors for N_2O concentrations and fluxes in the remotely sensed data, while similar to CO_2, water temperature showed its predictive strength for the water quality datasets (Table 3). Overall, water quality data showed higher predictive performance for all three GHG concentrations and fluxes than remote-sensing data (Table 3). On the other hand, N_2O and CO_2 concentrations and fluxes were better predicted by all three datasets than CH_4 concentration and fluxes (Table 3).

3.2. Observed vs predicted median GHG concentrations and diffusive fluxes in the test dataset

Regression analysis of predicted versus observed annual median GHG concentrations and fluxes from the test dataset (not used in model construction) revealed notable trends across the input datasets and GHG types (Fig. A5). Generally, the models could reproduce catchment scale-measured median values of GHG concentrations and fluxes. However, the slopes of these relationships were mostly <1, indicating that the prediction of all three datasets mostly underestimated GHG concentrations and fluxes, especially the higher values (Fig. A5). Moreover, the degree of underestimation by the models depended on the type of input data and GHG type, ranging from 24 % to 72 % for all the GHGs and across all three input datasets (Fig. A5).

Remotely sensed vegetation indices and water quality datasets more accurately predicted CO_2 concentrations and fluxes, with the lowest underestimation (23 %) found for CO_2 concentrations. The remotely sensed dataset also better predicted CH_4 concentrations, while CH_4 fluxes were better predicted by the combined dataset resulting in the lowest underestimation (29 %). Compared to CO_2 and CH_4, the models from all three datasets performed better on average for N_2O concentrations and fluxes. The combined dataset showed the lowest underestimation for both N_2O concentrations and fluxes, with the degree of underestimation ranging from 10 to 15 % (Fig. A5).

3.3. Upscaled GHG concentrations and fluxes from rivers in Germany

The modeled riverine GHG concentrations and subsequent annual diffusive flux estimates for the 2934 individual catchments in Germany were highly spatially variable, ranging up to 4 orders of magnitude (Fig. 2). In comparison to available measured values in the GRiMeDB dataset (Stanley et al., 2023; Table A5), modeled CO_2 and CH_4 concentrations were significantly ($p < 0.05$) lower than the measured values, CH_4 fluxes were comparable, while modeled CO_2 fluxes were significantly higher than the measured values (Fig. A6). Focusing on individual GHGs, the catchment-scale annual median riverine GHG concentrations and fluxes ranged from 107 to 3484 μg L^{-1} and from 0.09 to 25.31 kg m^{-2} yr^{-1} for CO_2-C, from 0.09 to 33.85 μg L^{-1} and from −1.28–60.25 g m^{-2} yr^{-1} for CH_4-C and from 141 to 2151 ng L^{-1} and −4.25–13.84 g m^{-2} yr^{-1} for N_2O-N (Fig. 2). Similar to the median fluxes, catchment-specific stream surface areas were also highly variable, ranging from 592 to 1,215,778 m^2. Total annual riverine GHG fluxes for

Table 3
Summary of the top three most essential predictor variables (explaining >60 % of the variance) from the best-performing ML models. Also included is the mean absolute error (MAE) of the predicted riverine GHG concentrations and fluxes expressed as a percentage of the actual mean values from the 20 sites.

Dependent variables	Algorithm	r^2	MAE (% of measured mean)	Important predictor variables	Dataset
CO_2-C concentration (μg L^{-1})	xgbTree	0.55	5.6	NDWI, NDVI, GNDVI	Remote sensing
CH_4-C concentration (μg L^{-1})	xgbTree	0.44	87.8	NDII, NDVI, SR	Remote sensing
N_2O-N concentration (ng L^{-1})	xgbTree	0.54	6.7	NDVI, NDWI, NDII	Remote sensing
CO_2-C flux mg m^{-2} d^{-1}	xgbTree	0.33	7.6	NDWI, MSI, GNDVI	Remote sensing
CH_4-C flux mg m^{-2} d^{-1}	xgbTree	0.33	19.7	NDWI, GNDVI, NDVI	Remote sensing
N_2O-N flux mg m^{-2} d^{-1}	gbm	0.46	13.2	GNDVI, MSI, NDII	Remote sensing
CO_2-C concentration (μg L^{-1})	gbm	0.70	4.5	Water temperature, EC, DO	Water quality
CH_4-C concentration (μg L^{-1})	xgbLinear	0.53	68.9	NO_3, EC, DO	Water quality
N_2O-N concentration (ng $^{L-1}$)	rf	0.60	6.2	Water temperature, EC, DO	Water quality
CO_2-C flux mg m^{-2} d^{-1}	rf	0.55	6.3	Water temperature, EC, DO	Water quality
CH_4-C flux mg m^{-2} d^{-1}	rf	0.53	16.0	Water temperature, EC, DO	Water quality
N_2O-N flux mg m^{-2} d^{-1}	rf	0.61	10.9	Water temperature, EC, DO	Water quality
CO_2-C concentration (μg L^{-1})	gbm	0.72	4.5	Water temperature, EC, DO	Remote sensing & water quality
CH_4-C concentration (μg L^{-1})	rf	0.60	71.5	Water temperature, EC, DO	Remote sensing & water quality
N_2O-N concentration (ng $^{L-1}$)	rf	0.62	5.9	Water temperature, EC, DO	Remote sensing & water quality
CO_2-C flux mg m^{-2} d^{-1}	xgbTree	0.53	6.3	EC, DOC, DO	Remote sensing & water quality
CH_4-C flux mg m^{-2} d^{-1}	xgbLinear	0.54	15.3	DOC, DO, EC	Remote sensing & water quality
N_2O-N flux mg m^{-2} d^{-1}	rf	0.66	10.7	Water temperature, EC, DO	Remote sensing & water quality

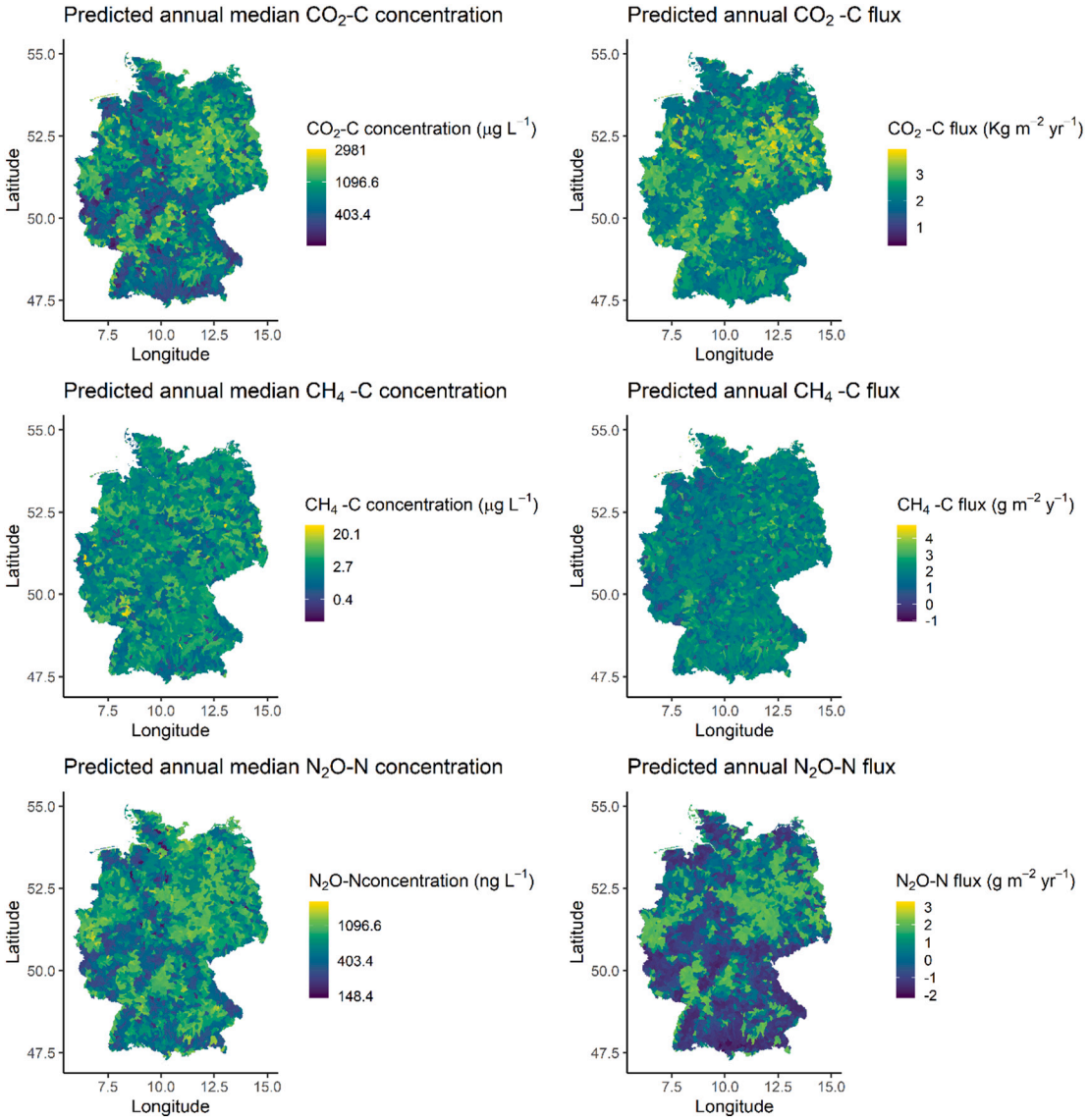

Fig. 2. Modeled annual riverine median GHG concentrations and estimated annual GHG diffusive fluxes for 2934 individual catchments in Germany for 2020.

the whole of Germany, quantified by multiplying these catchment-specific annual river surface areas and median fluxes, were 1216 Gg CO_2-C yr^{-1}, 0.80 Gg CH_4-C yr^{-1}, and 0.17 Gg N_2O-N yr^{-1}.

3.4. Effect of land use intensity on the spatial trends of total annual CO_2-equivalent fluxes

The modeled riverine CO_2-eq diffusive fluxes across the 2934 individual catchments in Germany ranged from 1.7 to 96.5 kg m^{-2} yr^{-1}, resulting in total annual fluxes of 4.56 Tg CO_2-eq yr^{-1} when all the catchment-specific fluxes are summed up (Fig. 3). CO_2 fluxes accounted for most of the fluxes (median for all catchments: 99 %), while CH_4 and N_2O were minor contributors. Catchment-scale land use appeared to account for the spatial variability in the total annual fluxes, with catchments with high annual fluxes coinciding with urban and arable-dominated regions (Fig. 3). Further analysis of the effect of land use at the catchment scale also revealed that land use intensity plays a significant role in the catchment-scale spatial heterogeneity in the daily riverine GHG fluxes (Fig. 4). Catchments dominated by urban areas and intensive cropland had significantly ($p < 0.05$) higher CO_2 and N_2O fluxes than those dominated by extensive cropland, forestry, and pasture. Compared to CO_2 and CH_4 (a decrease of up to 55 %), median N_2O fluxes showed the most significant decrease with changes in land use of up to 148 %, as the streams with the lowest fluxes (in forest and pasture-dominated catchments) became mostly N_2O sinks (Fig. 4).

4. Discussion

In this study, we demonstrate the potential of machine learning models driven by remotely sensed vegetation indices to spatially upscale riverine GHG diffusive fluxes to the national scale using limited field-based measurements. This research builds on previous studies that modeled riverine GHG fluxes over large spatial areas (Liu et al., 2022; Marzadri et al., 2021; Rocher-Ros et al., 2023) by additionally assessing how land use intensity accounts for catchment-scale spatial differences in the modeled fluxes from multiple catchments of different sizes (catchment areas: 0.1 to 489 km^2). Among the machine learning algorithms tested, complex decision-tree-based models such as rf, gbm, xgbTree, and xgbLinear outperformed other model structures (Table 2; Table 3), indicating complex relationships between the GHGs and their environmental controls. Although water quality input data predicted GHG concentrations and fluxes better than remotely sensed data, the difference in predictive strength based on the MAE of the two datasets was not substantial (Table 3). This finding suggested that the greater

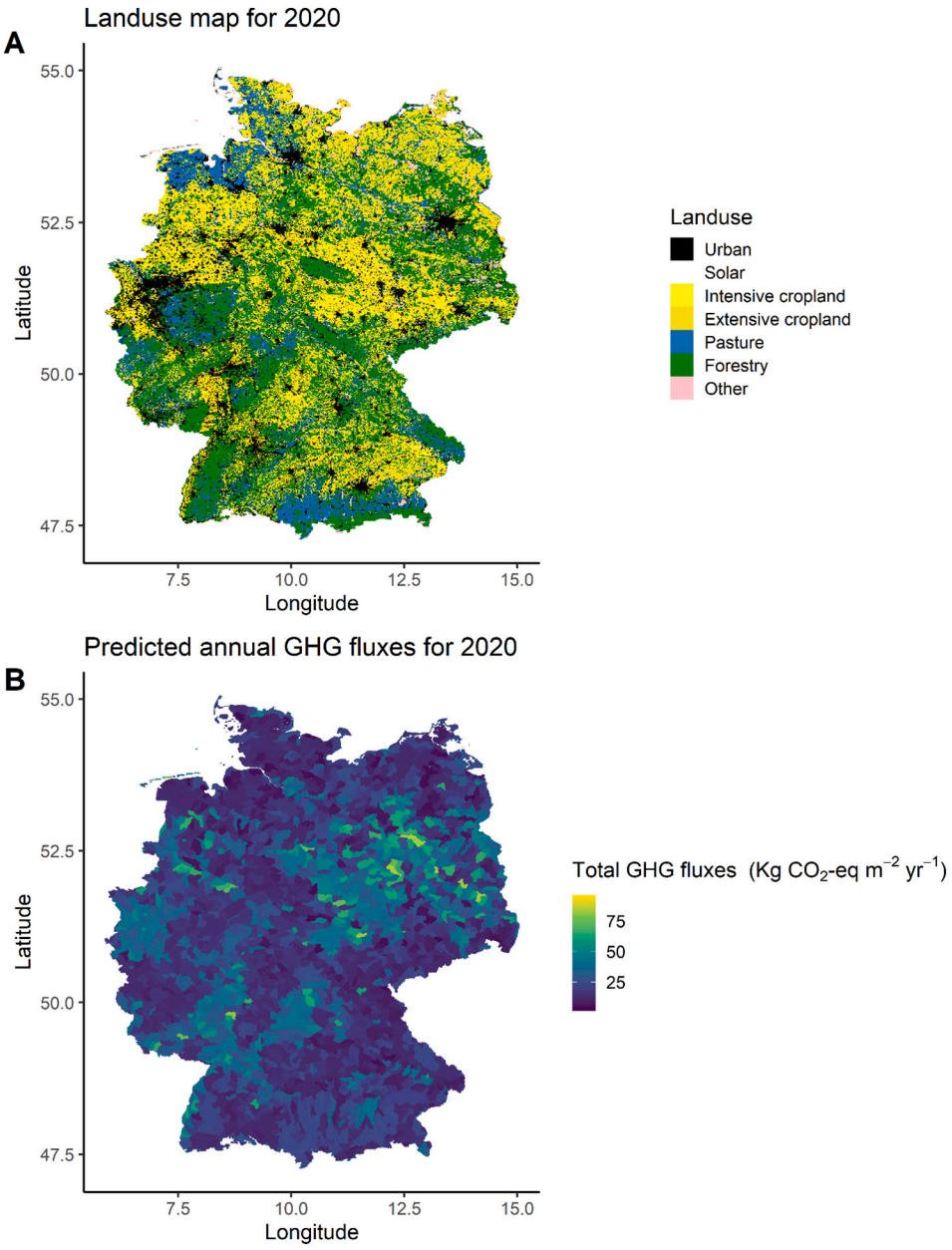

Fig. 3. a) Land use map for Germany for 2020, representing also differences in land use intensities across croplands. b) Total annual riverine CO_2 equivalent diffusive fluxes for the 2934 catchments in Germany for 2020.

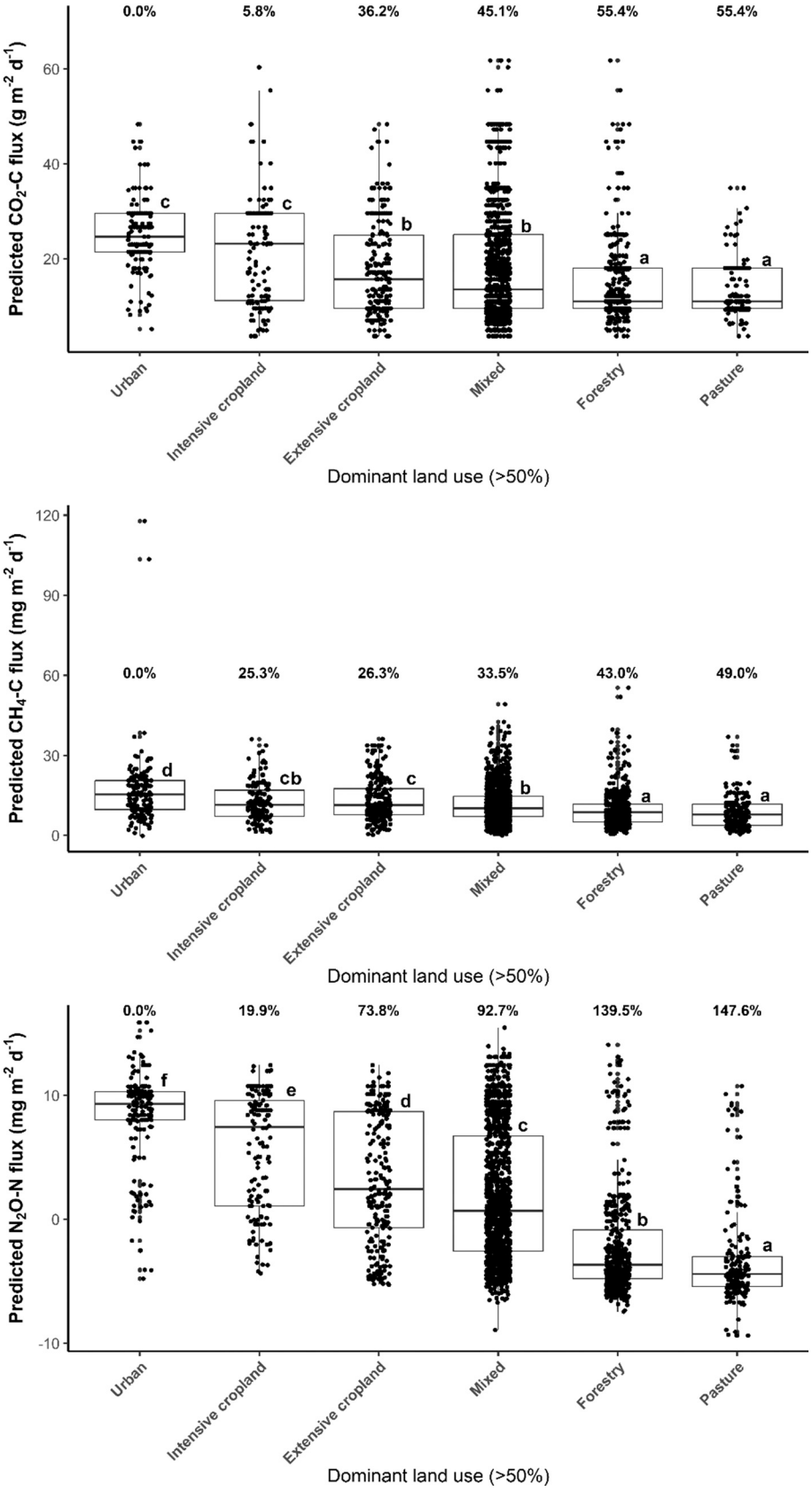

Fig. 4. Boxplots indicating the effect of land use on daily riverine diffusive GHG fluxes from individual catchments in Germany. The numbers on top of the boxplots indicate % declines in the median fluxes from the land use class with the highest fluxes to the land use class with the lowest fluxes. The letters on top represent significant differences ($p < 0.05$) from pairwise mean comparisons using the Wilcoxon test.

spatial availability of RS data, compared to water quality data, could be leveraged to upscale riverine emissions to larger areas. Applying this approach, the upscaled annual riverine CO_2-equivalent fluxes for all of Germany, based on national-scale remotely sensed vegetation indices as inputs, ranged from 1.65 to 96.37 kg m^{-2} yr^{-1} across 2934 individual catchments (Fig. 3). The highest diffusive GHG fluxes came from urban and intensive cropland-dominated catchments, while the lowest were from extensive cropland, forestry, and pasture-dominated catchments (Fig. 4).

4.1. Environmental controls of riverine GHG concentrations and diffusive fluxes

Similar to previous studies, decision tree-based models, such as the random forest and gradient boosting models, better predicted CO_2 concentrations and fluxes than other model structures (Liu et al., 2022; Xiong et al., 2024). Our results also showed that terrestrial and aquatic drivers are key to explaining the spatio-temporal variations in CO_2 concentrations and fluxes. For example, the best predictor of CO_2 included in-situ water quality parameters such as water temperature, electrical conductivity, DOC, and DO, which have previously been shown to indicate CO_2 production from temperature and nutrient-dependent in situ respiration of organic matter (Gómez-Gener et al., 2021; Mwanake et al., 2022, 2024). At the same time, vegetation quality and moisture indices from upstream catchment areas such as NDVI and NDWI were also important predictors of CO_2 concentrations and fluxes, indicating that terrestrial to aquatic transport of CO_2 originating from plant-mediated terrestrial respiration may have further enhanced in-situ CO_2 concentrations and fluxes in our studied streams. Several studies have reported similar mechanisms, linking terrigenous CO_2 concentrations to high riverine CO_2 fluxes during periods of stream-soil hydrological connectivity (Liu et al., 2023; Liu et al., 2022; Piatka et al., 2024). Such a conclusion is also supported by the prediction of instream CO_2 concentrations with vegetation moisture indices, which may indicate hydrological conditions within the catchments (Table 3).

Like CO_2 concentrations and fluxes, vegetation quality and moisture indices such as NDVI and NDWI were strong predictors of CH_4 concentrations and fluxes, suggesting that CH_4 sources in streams are closely linked to anaerobic respiration of soil-derived organic carbon or direct terrestrial inputs from riparian areas (e.g., Leng et al., 2021; Piatka et al., 2024; Rocher-Ros et al., 2023). Previous studies have also shown that CH_4 in streams can be produced via hydrogenotrophic or acetoclastic methanogenesis, using either CO_2 or acetic acid as carbon sources (Stanley et al., 2016). We argue that similar processes may explain the close links between CO_2 and CH_4 drivers. This conclusion is further supported by the prediction of CH_4 by water temperature, DO, DOC, and NO_3, relationships that have been linked with instream methanogenesis in the past (Baulch et al., 2011; Mwanake et al., 2023a; Schade et al., 2016).

Vegetation quality and moisture indices were also key to predicted instream N_2O concentrations and fluxes, suggesting that vegetation-mediated seasonal C and N cycling processes within catchments are closely linked to instream processes. Two opposing mechanisms may explain these findings. Firstly, seasonal (autumn and winter) reductions in vegetation cover resulting in reduced plant N uptake may result in excess terrestrial N that can end up in streams during hydrological connectivity, thus fueling in-situ N_2O production processes (e.g., Beaulieu et al., 2008; Herreid et al., 2021). Second, increases in vegetation cover and growth during summer may favor root exudates that promote terrestrial N_2O production, which may also be transported to streams during periods of hydrological connectivity (e.g., Piatka et al., 2024). Both mechanisms are supported by relationships of N_2O with water temperature, DO, NO_3, and DOC, which have been shown to be linked with instream or terrestrially sourced N_2O within fluvial ecosystems (Borges et al., 2018; Mwanake et al., 2019, 2023a; Wang et al., 2022).

Overall, water quality-driven ML models best predicted all three GHG concentrations and fluxes, with only slight improvements in predictive strength when the combined dataset incorporating remotely sensed data was used (Table 3). This finding suggests that water quality data more accurately reflects in-situ conditions governing fluvial GHG dynamics, as opposed to terrestrial characteristics derived from remotely sensed data. However, the differences in predictive strengths between the two datasets were mostly not substantial (model uncertainty differences <4 % for GHG fluxes), indicating that the extensive spatial availability of remotely sensed data could be leveraged to upscale fluvial GHG fluxes from catchment-scale field measurements to larger regional or nationwide estimates. This approach was demonstrated in this study for Germany and aligns with a few previous studies that used machine-learning algorithms with remotely sensed data to upscale catchment-scale GHG measurements on much larger global scales (Marzadri et al., 2021; Rocher-Ros et al., 2023).

4.2. Comparison of modeled riverine GHG diffusive fluxes in Germany to regional and global estimates

To validate our modeled annual riverine GHG fluxes for Germany, we compared them to a few measured estimates from the temperate region and globally sampled across an entire year, thus also accounting for seasonality (Table 4). In terms of annual riverine emissions, our estimate for Germany of 4.56 Tg CO_2-eq yr^{-1} accounts for 3.1 % of riverine

Table 4
Comparison of modeled riverine fluxes in this study to a few regional and global estimates.

Land use	Country	Number of study reaches	Data duration	CO_2-C flux (g m^{-2} d^{-1})		CH_4-C flux (mg m^{-2} d^{-1})		N_2O-N flux (mg m^{-2} d^{-1})		Reference
				Range	Mean	Range	Mean	Range	Mean	
Mixed streams	Germany	2934	Annual, 2020	0.8–70.8	17.1	−3.5–165.1	11.4	−11.7–37.9	1.2	This study
Mixed streams	Germany	2	Annual, 2013–2020				10.1			Leng et al., 2021
Mixed streams	USA	3	Annual, 2012		0.4–1.1		6–43.8		−0.6–6.0	Schade et al., 2016
Mixed streams	Switzerland	1	Annual, 2016	13.3–494.5	31					Horgby et al., 2019a
Mixed streams	Europe	34	Annual, 2017	−0.8–5.8						Attermeyer et al., 2021
Mixed streams	Global				2.9		100.8		3.1	Li et al., 2021
Mixed streams	Global							−0.6–178.6		Hu et al., 2016
Mixed streams	Global					−125–5190	99			Stanley et al., 2016

emissions from Europe (median: 147. 1 Tg CO_2-eq yr^{-1}; Lauerwald et al., 2023), a percent equal to a third of its land mass area in Europe (Eu27). Our modeled daily diffusive riverine CO_2, CH_4, and N_2O fluxes for Germany are within the range of measured estimates from similar temperate streams in Germany, the USA, Switzerland, and Europe that drain mixed land uses (Table 4). Additionally, the upscaled annual riverine CO_2, CH_4, and N_2O fluxes in this study are also within the range of current field-based global estimates of −0.54–32 kg CO_2-C m^{-2} yr^{-1}, −0.22–65.18 g N_2O-N m^{-2} yr^{-1} and −0.59–17 kg CH_4-C m^{-2} yr^{-1} (Horgby et al., 2019b; Hu et al., 2016; Stanley et al., 2023). Taken together, the comparable nature of modeled fluxes in this study to other regional and global estimates further highlights the applicability of this upscaling technique across a wide range of streams characterized by different catchment characteristics (stream size, topography, land use, and climate).

4.3. Effects of land use intensities on modeled riverine GHG fluxes for Germany

Catchments within intensively managed land uses, as indicated by intensive croplands and urban areas, had up to 148 % higher modeled riverine GHG fluxes compared to those dominated by extensive croplands, as well as pasture and forested land uses, both with high or low management intervention (Fig. 4; Table A3). The link between increased GHG fluxes and intensively managed catchment land uses in this study agrees well with findings from previous studies based on actual field measurements and can be closely associated with nutrient, carbon, and dissolved GHG inputs to the streams from the surrounding soils (Brown et al., 2023; Herreid et al., 2021; Mwanake et al., 2023b, 2024; Park et al., 2023). For example, intensively managed cropland catchments may contribute higher nutrient inputs in streams than extensively managed catchments due to differences in the amounts of fertilizer applied, which can drive elevated instream respiration, nitrification, and denitrification in them, thus favoring instream CO_2 and N_2O production (e.g., Masese et al., 2017; Piatka et al., 2021; Wang et al., 2024). On the other hand, the presence of wastewater treatment plants in urban areas may result in nutrient, labile carbon, and dissolved GHG inputs to streams, also favoring elevated riverine GHG fluxes (e.g., Peterse et al., 2024; Xu et al., 2024). In contrast, streams in forested and pasture areas may receive fewer nutrient inputs due to better retention in the soils, lower nitrogen inputs, reduced labile carbon inputs, and decreased dissolved GHG concentrations inputs, resulting in much lower riverine GHG fluxes. We argue that similar mechanisms accounted for the significant differences that we found in our modeled riverine fluxes across land use classes (Fig. 4). This is further supported by the strong links between GHG concentrations and fluxes and vegetation quality and moisture indices, which may act as predictors for nutrient, organic matter, and hydrological conditions within the catchment soils (e.g., Wangari et al., 2023).

4.4. Sources of uncertainties and limitations of our upscaling methodology

Despite the potential demonstrated in this study for modeling national-scale riverine GHG fluxes comparable to regional and global measured estimates (Table 4), our modeled fluxes for Germany may have several sources of uncertainty. For example, the uncertainties in modeled diffusive fluxes from RS data (MAE as a percentage of the measured mean) were ±7.6 % for CO_2 fluxes, ±19.7 % for CH_4 fluxes, and ±13.2 % for N_2O fluxes. When combined with the uncertainty in k values used to compute the diffusive fluxes in the training dataset (±10.0 %; Raymond et al., 2012), the cumulative uncertainties in the diffusive fluxes, based on error propagation, were ±12.5 % for CO_2 fluxes, ±22.1 % for CH_4 fluxes, and ±16.6 % for N_2O fluxes. Regarding areal fluxes, we estimate total uncertainties in stream surface area quantification to be larger than the flux uncertainties, driven by the failure to account for seasonal expansion and contraction in river surface areas due to using fixed annual surface areas (uncertainty ~28 %; Mwanake et al., 2022) and the computation of stream width from long-term discharge (uncertainty ~4 %; Xu et al., 2020). By combining these two uncertainties for surface area estimation (±32 %), the uncertainties in areal riverine diffusive fluxes, based on error propagation, are ±34.35 % for CO_2 fluxes, ±38.98 % for CH_4 fluxes, and ±36.05 % for N_2O fluxes. Since the total CO_2-equivalent fluxes were largely dominated by CO_2 (>95 %), applying the cumulative uncertainty for CO_2 (±34.35 %) to the riverine emissions for Germany (4.56 Tg CO_2-eq yr^{-1}) results in a range of 3.01 to 6.11 Tg CO_2-eq yr^{-1}. Other uncertainties that were challenging to account for quantitatively suggest that these quantified fluxes may primarily underestimate the overall fluxes for Germany. For instance, the failure of our upscaling methodology to account for spatial hot spots along river reaches (e.g., Koschorreck et al., 2024; Mwanake et al., 2024), temporal hot moments such as peak night time CO_2 fluxes, (e.g., Attermeyer et al., 2021; Koschorreck et al., 2024; Woodrow et al., 2024) and extremely high seasonal fluxes due to peak precipitation events (e.g., Mwanake et al., 2022; Piatka et al., 2024). In addition, the inclusion of only diffusive fluxes and, therefore, also underestimating CH_4 emissions, particularly due to the significant contribution of ebullition, as shown in previous studies (Baulch et al., 2011; Michaelis et al., 2024; Wilkinson et al., 2019).

Another important source of uncertainty on the modeled fluxes worth highlighting is the spatial limitation of the training data, which was skewed towards a few headwater streams, despite German streams and rivers being highly diverse, including very small streams to large estuary rivers (See Premke et al., 2022). This limitation was largely driven by the paucity of the existing riverine GHG datasets for Germany in space and time, as shown by the GRiMe database, which represented the only available compiled data for stream GHG concentration and fluxes in Germany for an out-of-bag validation of our modeled estimates. The lack of the required temporal coverage (annual) (Table A5) at spatially diverse sites to properly validate our modeled fluxes may partly explain the significant differences between measured and predicted values (Fig. A6), which were not apparent when we used median values for our 20 training catchments sampled throughout the year (Fig. A7). Despite the spatial limitation of our training data, its skewness towards headwater streams may have helped minimize the effects of the uncertainties introduced in the overall countrywide flux estimates due to this limitation. Headwater streams have been shown to occupy 89 % of global fluvial lengths (Raymond et al., 2013) and contribute over 70 % of fluvial GHG fluxes, compared to large rivers (Li et al., 2021). Therefore, including these streams in the training data ensured the representation of ecosystems with the largest influence on overall fluvial fluxes.

5. Conclusions

In this study, the modeling of riverine GHG fluxes using ML with remotely sensed data provided an alternative for upscaling riverine GHG fluxes in the absence of adequate water quality data in space and time. The ability of such a modeling approach to directly predict catchment scale diffusive fluxes also overcomes the need to additionally model gas exchange rates separately (See Raymond et al., 2012), reducing the overall uncertainties in upscaled fluxes, particularly over large spatial scales. In addition to these methodological improvements, our upscaled GHG fluxes revealed the importance of land use intensities in accounting for catchment-scale differences in the riverine fluxes. For instance, intensively managed croplands had much higher CO_2 and N_2O fluxes than extensively managed croplands, which we closely linked to the differences in amounts of N-based fertilizer inputs. However, our modeled fluxes had several uncertainties highlighted above, calling for improvement of future upscaling exercises using this methodology to better quantify this important GHG source at national scales for proper GHG accounting. This improvement will involve more spatially distributed monitoring sites across countries to properly calibrate and

validate the ML models and their outputs, producing more accurate and reliable estimates on a national scale.

Glossary

Not applicable.

Abbreviations

Not applicable.

Data availability

The entire dataset for model training and validation is available at Mwanake, 2023 (doi:10.35097/1684).

CRediT authorship contribution statement

R.M. Mwanake: Writing – review & editing, Writing – original draft, Visualization, Formal analysis, Data curation, Conceptualization. **E.G. Wangari:** Writing – review & editing, Data curation. **K. Winkler:** Writing – review & editing, Data curation. **G.M. Gettel:** Writing – review & editing, Supervision, Funding acquisition. **K. Butterbach-Bahl:** Writing – review & editing, Supervision, Funding acquisition. **R. Kiese:** Writing – review & editing, Supervision, Funding acquisition, Conceptualization.

Funding sources

Infrastructure for the research was provided by the TERENO Bavarian Alps/Pre-Alps Observatory, funded by the Helmholtz Association through the joint program Changing Earth – Sustaining our Future (ATMO - PoF IV) program of Karlsruhe Institute of Technology (KIT). KBB received additional funding by the Danish National Research Foundation (DNRF), Grant Number P2 "Pioneer Center for Research in Sustainable Agricultural Futures (Land-CRAFT).

Declaration of competing interest

The authors declare no conflict of interest.

Acknowledgments

The authors would like to thank the entire laboratory staff at Karlsruhe Institute of Technology, Campus Alpin, Justus Liebig University Giessen, and the University of Tübingen for helping to provide logistical support and for supporting the gas and nutrient analyses that yielded the modeling dataset.

Appendix A

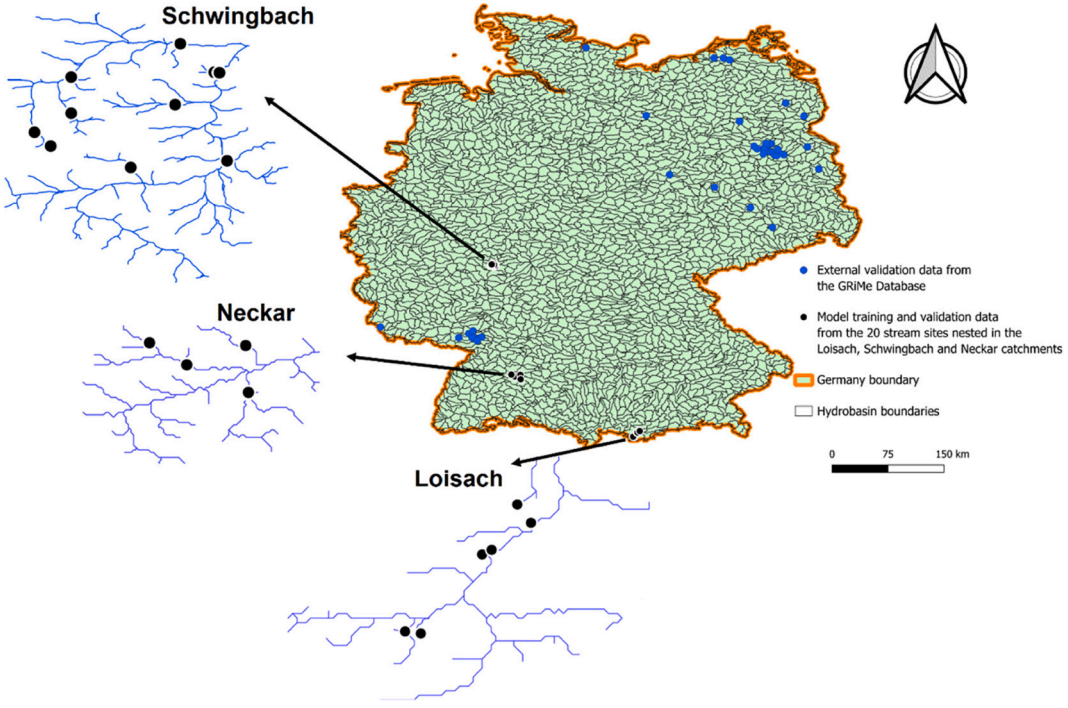

Fig. A1. German map showing 2934 catchments from the global hydrobasin dataset (Level 12; retrieved July 1, 2024: https://www.hydrosheds.org/products/hydrobasins). The black dots show the 20 stream sites nested within the Schwingbach, Neckar, and Loisach catchments used for model training and validation. The blue dots show the external validation sites from the GriMe database that were not used during the model construction phase (Stanley et al., 2023).

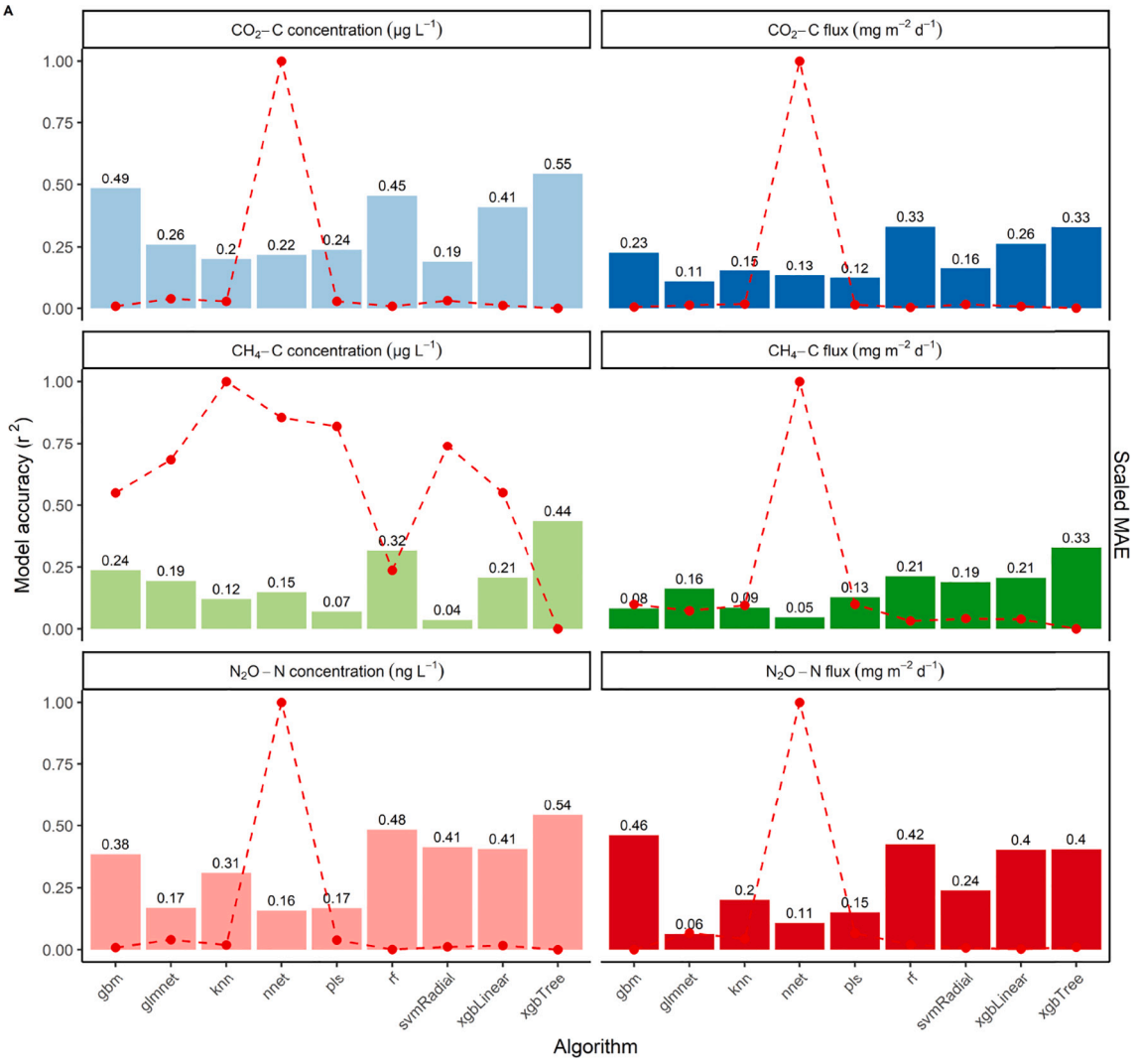

Fig. A2. Performance of several ML algorithms (Table 1) in predicting GHG concentration and fluxes from remotely sensed vegetation indices alone. Bars and text show the r^2, while the red line and dots show the mean absolute error (scaled from 0 to 1).

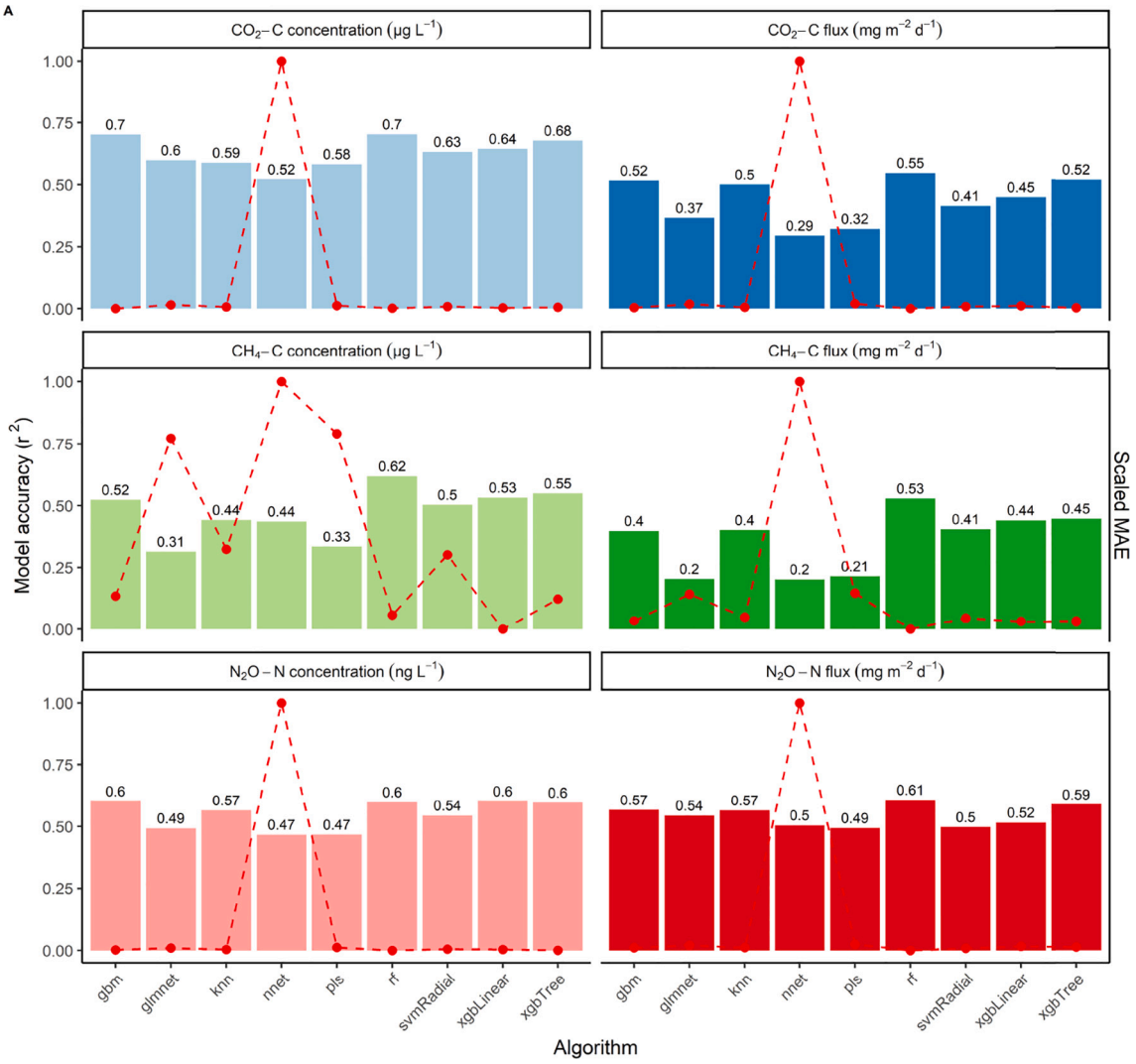

Fig. A3. Performance of several ML algorithms (Table 1) in predicting GHG concentration and fluxes from the in-situ water quality data alone. Bars and text show the r^2, while the red line and dots show the mean absolute error (scaled from 0 to 1).

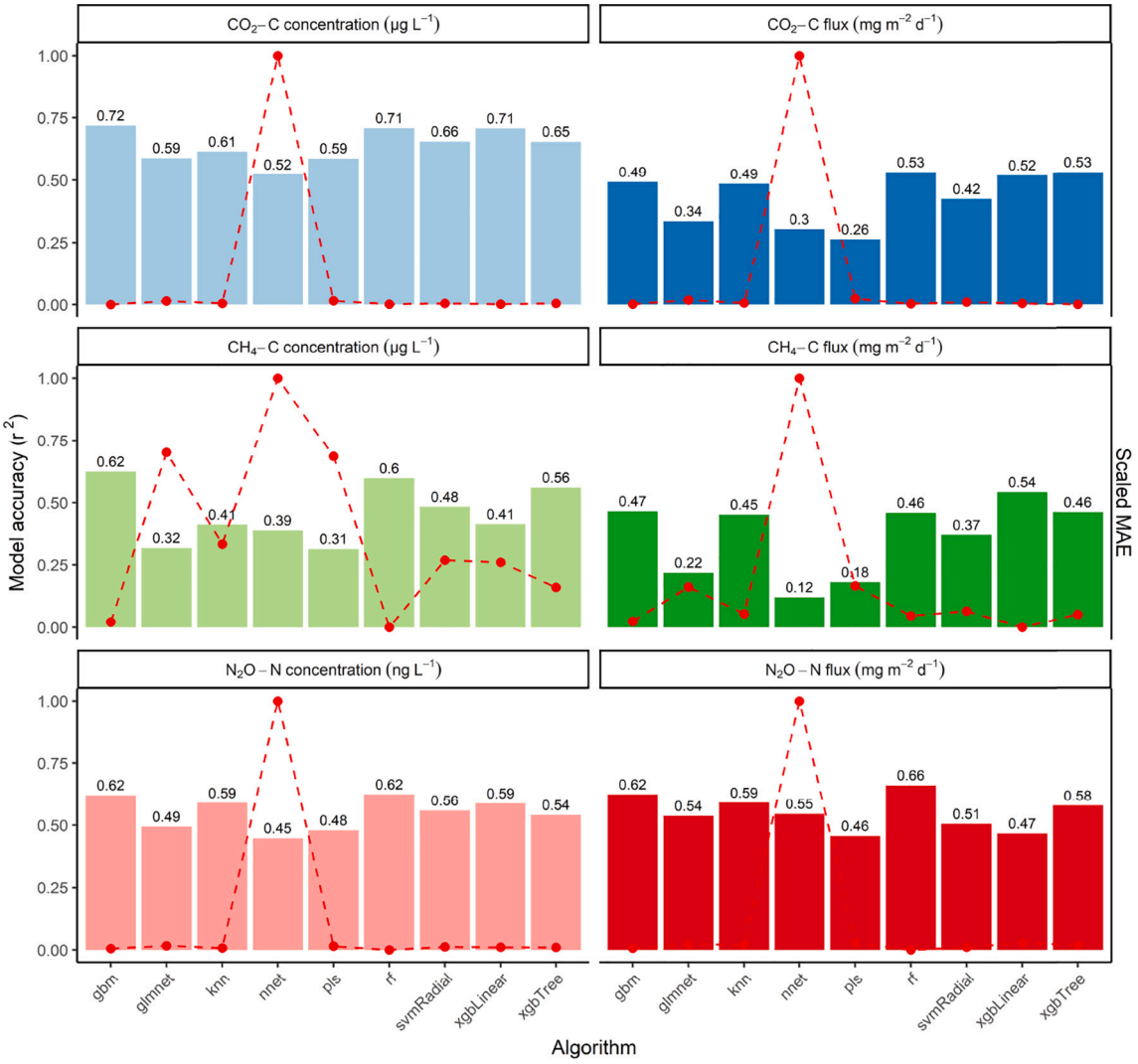

Fig. A4. Performance of several ML algorithms (Table 1) in predicting GHG concentration and fluxes from the combined in situ water quality data and remotely sensed vegetation indices. Bars and text show the r^2, while the red line and dots show the mean absolute error (scaled from 0 to 1).

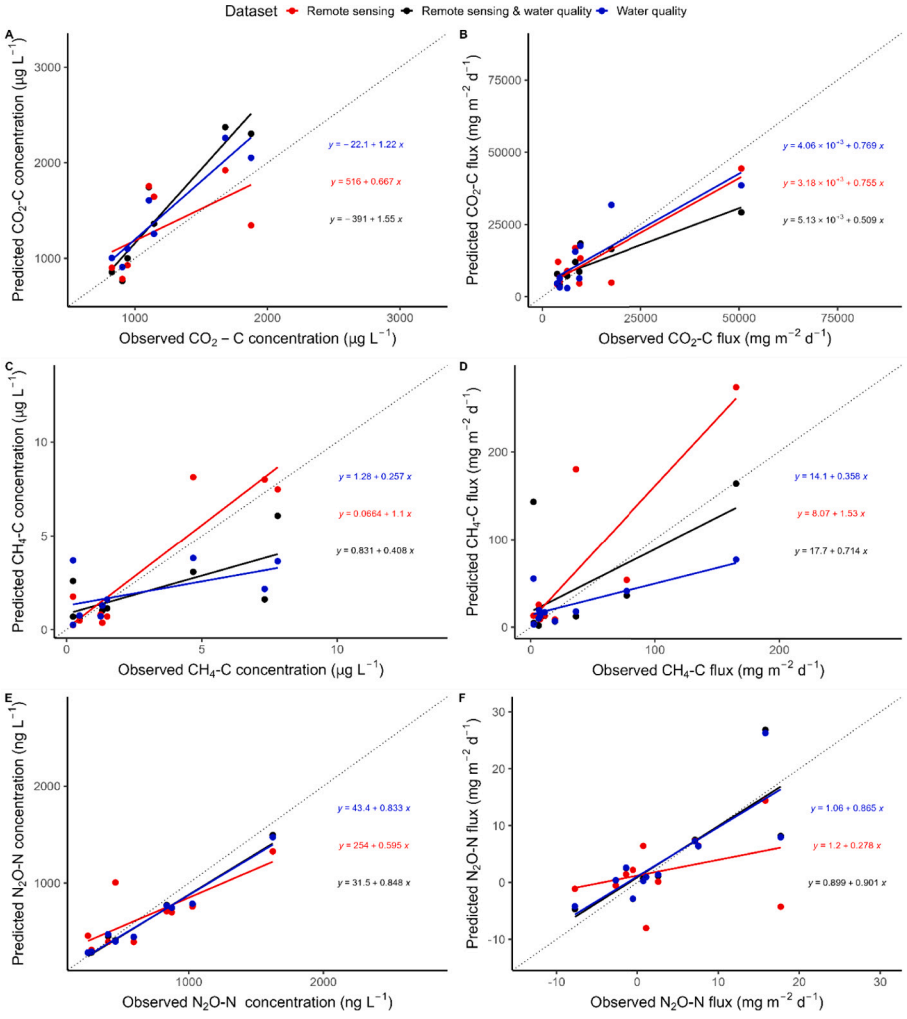

Fig. A5. Regression analysis of the observed versus the predicted annual median riverine GHG concentrations and fluxes from 20 % of the data not used in model construction. The different colors show predictions from the RS dataset (red), WQ dataset (blue), and a combination of both (black), while different shapes indicate seasons. The text on the graph represents the equation of the significant relationships ($p < 0.05$).

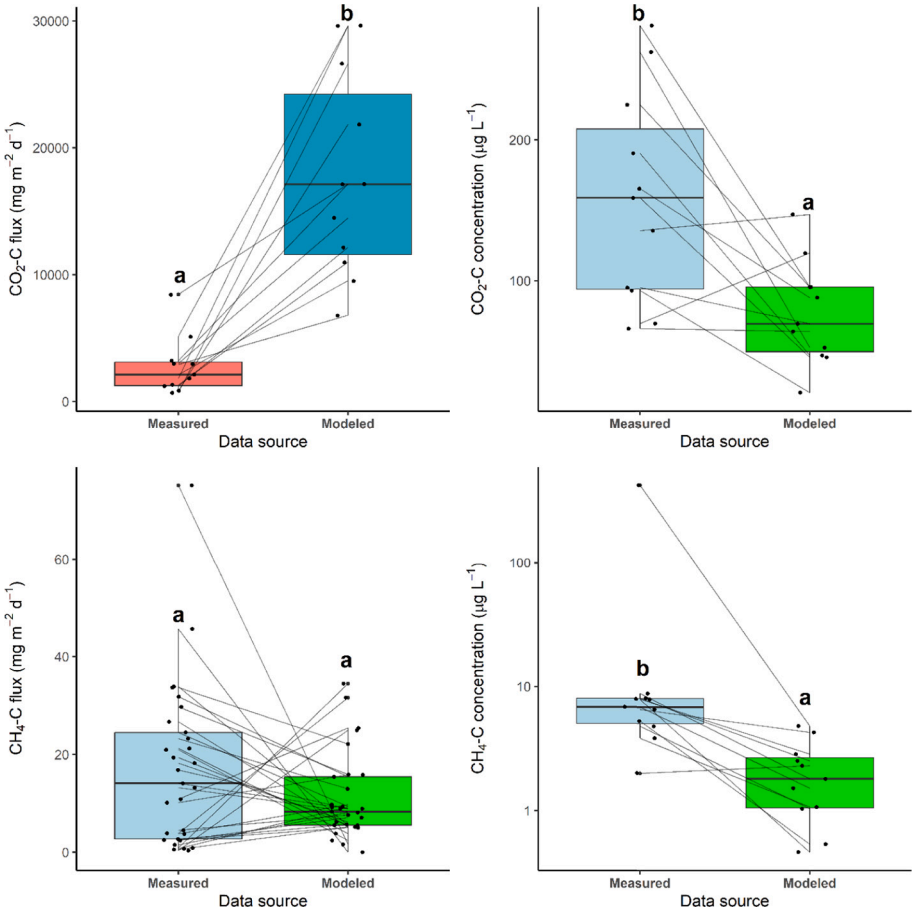

Fig. A6. Comparison of modeled (2020 German maps) and actual field measurements of GHG concentrations and fluxes from the GRiMe database (Stanley et al., 2023; Table A5). The letters on top represent significant differences from pairwise mean comparisons using the Wilcoxon test. Lines indicate catchment pairwise comparisons.

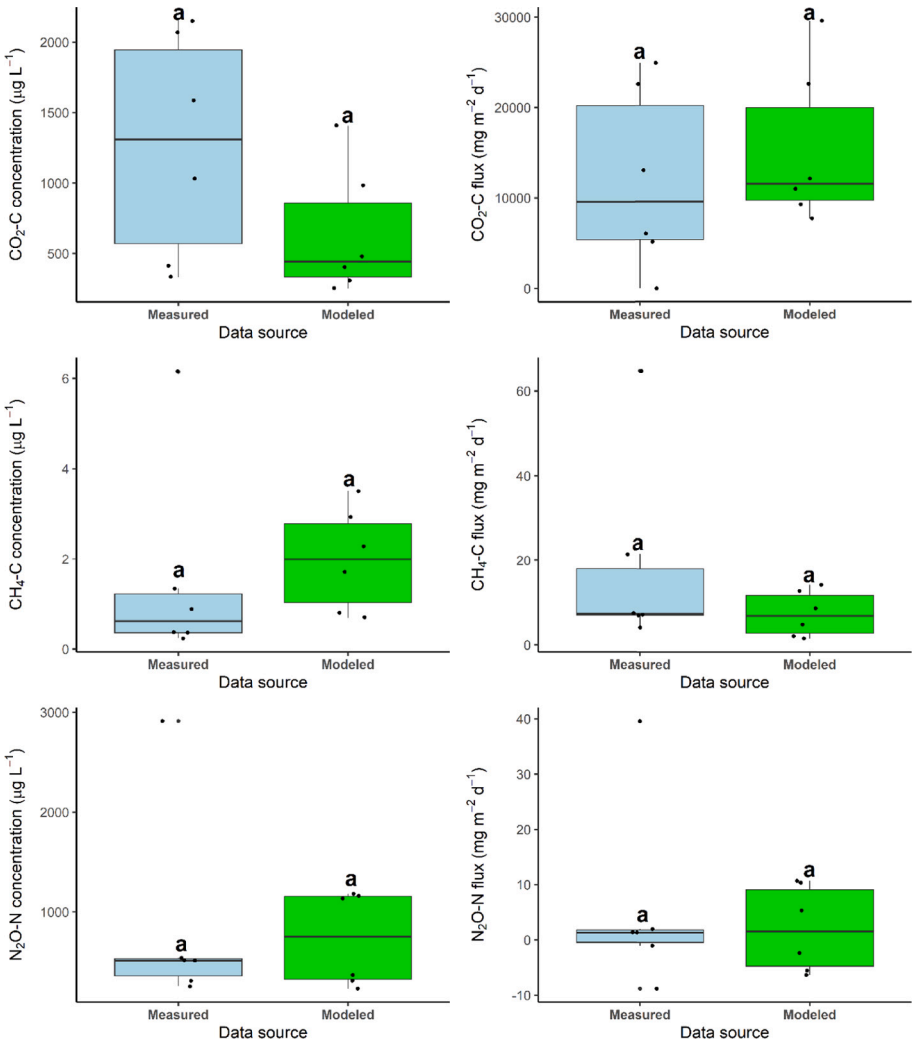

Fig. A7. Comparison of modeled (2020 German maps) and actual field measurements of GHG concentrations and fluxes from the 20 sites used in model construction. The letters on top represent significant differences from pairwise mean comparisons using the Wilcoxon test.

Table A1
Summary statistics for the measured parameters from the 20 catchments.

Variable	Mean ± SE	Min–max
Water temperature	10.75 ± 0.33	0.9–23.8
Electrical conductivity (µs cm^{-1})	659.16 ± 26.2	240–1718
pH	8.02 ± 0.03	7.17–8.82
DO (mg L^{-1})	10.01 ± 0.16	5.43–15.69
DO saturation	96.94 ± 1.33	54.6–143
NH_4-N (mg L^{-1})	0.09 ± 0.01	0–0.45
NO_3-N (mg L^{-1})	3.2 ± 0.26	0.04–12.84
DOC (mg L^{-1})	3.44 ± 0.16	1.13–16.05
CO_2-C concentration (µg L^{-1})	1135.03 ± 66.14	219.96–3861
CH_4-C concentration (µg L^{-1})	2.82 ± 0.54	0.12–51.6
N_2O-N concentration (ng L^{-1})	830.91 ± 63.34	19.6–4424
CO_2-C flux g m^{-2} d^{-1}	18.43 ± 2.35	−0.73–174.34
CH_4-C flux mg m^{-2} d^{-1}	31.67 ± 4.1	0–307.83
N_2O-N flux mg m^{-2} d^{-1}	12.09 ± 2.2	−18.52–162.84

Table A2
Spatial datasets used to generate harmonized land use map for Germany.

Dataset	Description, classes used	Spatial resolution	Reference year	Source
HILDA+ land use 2020	Global land use/cover map with urban, cropland, tree crops, agroforestry, pasture, forest, unmanaged grass and shrublands.	1 × 1km	2020	updated version from Winkler et al., 2021
Dou et al. European land system map	Land system classes and intensities (low – medium – high): • forest types (based on wood production and primary forest probability) • grasslands (based on grazing, nitrogen input and mowing frequency) • croplands (based on nitrogen inputs and field size)	1 × 1 km	ca. 2018	Dou et al., 2021
CORINE land cover map	European land cover map with cropland, pasture, and forest types	100 × 100 m	2018	Copernicus Land Monitoring Service, 2020
Preidl et al. land cover map	German land cover map with detailed crop types (wheat, barley, legumes, maize, potato, rapeseed, etc.)	20 × 20 m	2016	Preidl et al., 2020
Blickensdörfer et al. crop type map	German crop type classification (wheat, barley, potato, maize, rapeseed etc.)	10 × 10 m	2019	Blickensdörfer et al., 2022
High nature value (HNV) farmland	Map of extensive farming systems with high biodiversity value	100 × 100 m	2012	EEA, 2017
Agraratlas: organic farming areas	Share of organically farmed area in utilized agricultural area in 2020 in a grid with a width of 5 km	5 × 5 km	2020	Destatis, 2021
German renewable energy sites	Locations and system data of renewable energy systems: bioenergy plants and open-space photovoltaics		2020	Manske et al., 2022

Table A3
Aggregated and detailed land use classes and definitions from the harmonized German land use map.

Aggregated land use class	Detailed land use class	Description/definition
Intensive cropland (high fertilization: ca. 250 kg N/ha; potentially irrigated)	Intensive C3 cereal crops	Intensive cereal cultivation (wheat, rye, barley, etc.) for food production
	Intensive C3 oil crops	Intensive oil crops (rapeseed, sunflower, linseed, soybeans) for food production
	Intensive C3 fruit and vegetables	Intensive fruit or vegetable crops (leeks, onion, carrots, strawberries, grape etc.) for food production
	Intensive C3 starchy roots	Intensive starchy root crops (potatoes, sugar beet) for food production
	Intensive C4 crops	Intensive maize cultivation for food production
	Intensive C3/C4 fodder crops	Intensive crops (cereals, starchy roots, maize) cultivated for feeding domestic livestock
	Bioenergy gen. 1	Food crops (rapeseed, wheat, barley, maize, sugar beet) cultivated for bioenergy production (high fertilization: ca. 250 kg N/ha; potentially irrigated)
	Bioenergy gen. 2	Non-food crops or grass used in the production of biofuels or biomass, e.g. miscanthus, short rotation coppice willow (low fertilization: ca. 100 kg N/ha; rainfed)
Extensive cropland (low fertilization: ca. 100 kg N/ha; rainfed)	Extensive C3 cereal crops	Extensive cereal cultivation (wheat, rye, barley, etc.) for food production
	Extensive C3 oil crops	Extensive oil crops (rapeseed, sunflower, linseed, soybeans) for food production
	Extensive C3 fruit and vegetables	Extensive fruit or vegetable crops (leeks, onion, carrots, strawberries, grape etc.) for food production
	Extensive C3 pulses	Extensive pulses cultivation (peas, lentils, chickpeas, beans) for food production
	Extensive C3 starchy roots	Extensive starchy root crops (potatoes, sugar beet) for food production
	Extensive C4 crops	Extensive maize cultivation for food production
	Extensive C3/C4 fodder crops	Extensive crops (cereals, starchy roots, maize) cultivated for feeding domestic livestock
	Sustainable arable	Very extensive (organic) farming (cereal, pulses, starchy roots, fruit and vegetables) for food production
Pasture	Intensive pastoral	Intensive pasture for livestock (frequent mowing, high fertilization, no grazing)
	Extensive pastoral	Extensive pasture for livestock (moderate mowing and/or moderate grazing)
	Very extensive pastoral	Very extensive pasture for livestock (only low grazing, e.g. mountain areas)
Forestry	Agroforestry	Agroforestry systems with a mix of broadleaf trees and crop cultivation (cereals, fruit and vegetables, oil crops)
	Broadleaf forest (intensive)	Broadleaf trees with intensive forest management
	Conifer forest (intensive)	Conifer trees with intensive forest management
	Broadleaf forest (extensive)	Broadleaf trees with extensive forest management
	Conifer forest (extensive)	Conifer trees with extensive forest management
	Multifunctional mixed woodland (extensive)	Mixed trees with extensive forest management
	Conserved woodland	Protected forests with no/low management
Solar	Dedicated solar farm	Large-scale installation of solar panels for solar energy production
	Agrovoltaic farm	Combination of cropland (cereals, maize, starchy roots or fruit and vegetables) or pasture and solar energy production
Urban	Urban	Urban areas, settlements, built-up surfaces and infrastructure
Other	Other	Unlabeled, sparsely or unmanaged land (mining areas, wetlands, shrubs, barren land, rocks and ice)
	Water	Water bodies

Table A4
National land use statistics for Germany in 2020 used for land use map calibration.

Land use areas	Derived values and units	Source
Forest area	107,000 km^2	Destatis (2024)
Cropland area	118,000 km^2	BMEL (2022)
Pasture area	47,000 km^2	BMEL (2022)
Urban area	51,800 km^2	Destatis (2024)

Table A5
Characteristics of the external validation dataset from the GRiMe database (Fig. A1; Stanley et al., 2023). Source ID and Site IDs can be looked up under the GRiMe Database.

Source ID	Site ID	Land use	Sampling dates	Longitude	Latitude	ID in the 2934 catchments
2223	1004	Urban	2020-03-15	7.979	49.214	2121141740
2223	1005	Urban	2020-03-15	8.299	49.1908	2120449820
2223	1006	Urban	2020-03-15	8.156	49.284	2120446210
2223	1007	Urban	2020-03-15	8.377	49.2238	2120447840
2223	1008	Urban	2020-03-15	8.2252	49.2463	2120446310
2223	1009	Urban	2020-03-15	8.2295	49.3308	2120446210
2223	1010	Urban	2020-03-15	8.2171	49.2096	2120449820
2223	1011	Urban	2020-03-15	8.3015	49.1615	2120449970
2223	3204	Urban	2020-03-15	7.97832	49.213	2121141740
2223	3205	Urban	2020-03-15	8.296	49.192	2120449820
2223	3206	Urban	2020-03-15	8.1536	49.2845	2120446210
2223	3207	Urban	2020-03-15	8.3753	49.2236	2120447840
2223	3208	Urban	2020-03-15	8.2244	49.246	2120446310
2223	3209	Urban	2020-03-15	8.2255	49.3319	2120446210
2223	3210	Urban	2020-03-15	8.2126	49.2102	2120449820
2223	3211	Urban	2020-03-15	8.2984	49.1607	2120449970
2251	1383	Urban	2020-04-15	13.6886	52.4298	2120366350
2251	1384	Urban	2020-04-15	13.3196	52.5194	2120363970
2251	1385	Urban	2020-04-15	13.2162	52.5362	2120363970
2251	1386	Urban	2020-04-15	13.1651	52.5782	2120361600
2251	1387	Urban	2020-04-15	13.4396	52.4895	2120363970
2251	1388	Urban	2020-04-15	13.497	52.4705	2121109280
2251	1389	Urban	2020-04-15	13.3667	52.5366	2120363450
2251	1390	Urban	2020-04-15	13.3264	52.4433	2120367060
2251	1391	Urban	2020-04-15	13.5204	52.4264	2121109720
2251	1392	Urban	2020-04-15	13.3859	52.5821	2120363450
2251	1393	Urban	2020-04-15	13.3492	52.5649	2120363450
2251	1394	Urban	2020-04-15	13.4688	52.6238	2121108460
2251	1395	Urban	2020-04-15	13.4531	52.6288	2121108460
2251	1396	Urban	2020-04-15	13.6124	52.4589	2120365810
2251	1397	Urban	2020-04-15	13.4109	52.6207	2120363450
2251	1398	Urban	2020-04-15	13.5628	52.4151	2120366100
2251	1399	Urban	2020-04-15	13.5796	52.5259	2121109720
2251	1400	Urban	2020-04-15	13.3754	52.6316	2120363300
2265	1652	Mixed	2020-08-10 to 2020-10-26	13.485	51.152	2120400520
2265	1653	Mixed	2020-08-10 to 2020-10-26	13.1	51.5	2120390270
2265	1654	Mixed	2020-08-10 to 2020-10-26	12.47	51.86	2120382220
2265	1655	Mixed	2020-08-10 to 2020-10-26	11.68	52.08	2120372860
2265	1656	Mixed	2020-08-10 to 2020-10-26	11.27	53.12	2120348790
2334	9286	Wetland	2020-04-01 to 2020-09-29	12.46061	54.13348	2121094130
2334	9287	Wetland	2020-04-01 to 2020-09-29	12.62399	54.13312	2121094130
2334	9288	Wetland	2020-04-01 to 2020-09-29	12.73745	54.0998	2120329020
2334	9289	Wetland	2020-04-01 to 2020-09-29	12.73626	54.09996	2120329020
7157	7762	Mixed	2020-09-05	6.6	49.4	2121138900
7267	8519	Forest	2020-01-20	14.1	52.57	2121108590
7267	8520	Forest	2020-01-20 to 2020-10-17	12.91	53.02	2120351970
7267	8522	Agricultural	2020-01-20 to 2020-10-17	14.04	53.11	2120347990
7267	8523	Agricultural	2020-01-20 to 2020-10-17	13.72	53.34	2120344040
7267	8524	Agricultural	2020-01-20 to 2020-10-17	14.3	52.18	2120373270
11894	11890	Forest/wetland	2020-08-17 to 2020-08-18	10.211	54.314	2120025550

Data availability

The datasource has been included in the manuscript.

References

Aho, K.S., Raymond, P.A., 2019. Differential response of greenhouse gas evasion to storms in forested and wetland streams. J. Geophys. Res. Biogeo. 124 (3), 649–662. https://doi.org/10.1029/2018JG004750.

Attermeyer, K., Casas-Ruiz, J.P., Fuss, T., Pastor, A., Cauvy-Fraunié, S., Sheath, D., Nydahl, A.C., Doretto, A., Portela, A.P., Doyle, B.C., Simov, N., Gutmann Roberts, C.,

Niedrist, G.H., Timoner, X., Evtimova, V., Barral-Fraga, L., Bašić, T., Audet, J., Deininger, A., Bodmer, P., 2021. Carbon dioxide fluxes increase from day to night across European streams. Communications Earth & Environment 2 (1), 118. https://doi.org/10.1038/s43247-021-00192-w.

Bai, Y., Cai, W., He, X., Zhai, W., Pan, D., Dai, M., Yu, P., 2015. A mechanistic semi-analytical method for remotely sensing sea surface pCO_2 in river-dominated coastal oceans: a case study from the East China Sea. J. Geophys. Res. Oceans 120 (3), 2331–2349. https://doi.org/10.1002/2014JC010632.

Bannari, A., Morin, D., Bonn, F., Huete, A.R., 1995. A review of vegetation indices. Remote Sens. Rev. 13 (1–2), 95–120. https://doi.org/10.1080/02757259509532298.

Bastviken, D., Sundgren, I., Natchimuthu, S., Reyier, H., Gälfalk, M., 2015. Technical note: cost-efficient approaches to measure carbon dioxide (CO_2) fluxes and concentrations in terrestrial and aquatic environments using mini loggers. Biogeosciences 12 (12), 3849–3859. https://doi.org/10.5194/bg-12-3849-2015.

Bastviken, D., Nygren, J., Schenk, J., Parellada Massana, R., Thanh Duc, N., 2020. Technical note: facilitating the use of low-cost methane (ch4) sensors in flux chambers-calibration, data processing, and an open-source make-it-yourself logger. Biogeosciences 17 (13), 3659–3667. https://doi.org/10.5194/bg-17-3659-2020.

Baulch, H.M., Dillon, P.J., Maranger, R., Schiff, S.L., 2011. Diffusive and ebullitive transport of methane and nitrous oxide from streams: are bubble-mediated fluxes important? Journal of Geophysical Research: Biogeosciences 116 (4). https://doi.org/10.1029/2011JG001656.

Beaulieu, J.J., Arango, C.P., Hamilton, S.K., Tank, J.L., 2008. The production and emission of nitrous oxide from headwater streams in the Midwestern United States. Glob. Chang. Biol. 14 (4), 878–894. https://doi.org/10.1111/j.1365-2486.2007.01485.x.

Begum, M.S., Bogard, M.J., Butman, D.E., Chea, E., Kumar, S., Lu, X., Nayna, O.K., Ran, L., Richey, J.E., Tareq, S.M., Xuan, D.T., Yu, R., Park, J.H., 2021. Localized pollution impacts on greenhouse gas dynamics in three anthropogenically modified Asian River systems. Journal of Geophysical Research: Biogeosciences 126 (5). https://doi.org/10.1029/2020JG006124.

Berrar, D., Lopes, P., Dubitzky, W., 2019. Incorporating domain knowledge in machine learning for soccer outcome prediction. Mach. Learn. 108 (1), 97–126. https://doi.org/10.1007/s10994-018-5747-8.

Blickensdörfer, L., Schwieder, M., Pflugmacher, D., Nendel, C., Erasmi, S., Hostert, P., 2022. Mapping of crop types and crop sequences with combined time series of Sentinel-1, Sentinel-2 and Landsat 8 data for Germany. Remote Sensing of Environment 269, 112831. https://doi.org/10.1016/j.rse.2021.112831.

Borges, A.V., Darchambeau, F., Lambert, T., Bouillon, S., Morana, C., Brouyère, S., Hakoun, V., Jurado, A., Tseng, H.C., Descy, J.P., Roland, F.A.E., 2018. Effects of agricultural land use on fluvial carbon dioxide, methane and nitrous oxide concentrations in a large European river, the Meuse (Belgium). Sci. Total Environ. 610–611, 342–355. https://doi.org/10.1016/j.scitotenv.2017.08.047.

Brown, A.M., Bass, A.M., Skiba, U., MacDonald, J.M., Pickard, A.E., 2023. Urban landscapes and legacy industry provide hotspots for riverine greenhouse gases: a source-to-sea study of the River Clyde. Water Res. 236, 119969. https://doi.org/10.1016/j.watres.2023.119969.

Bundesministerium für Ernährung und Landwirtschaft (BMEL), 2022. Daten und Fakten. Land-, Forst- und Ernährungswirtschaft mit Fischerei und Wein- und Gartenbau. https://www.bmel.de/SharedDocs/Downloads/DE/Broschueren/daten-fakten-2022.html.

Copernicus Land Monitoring Service, 2020. CORINE Land Cover 2018 (vector/raster 100 m), Europe, 6-yearly. URL: https://land.copernicus.eu/en/products/corine-land-cover/clc2018 (accessed 7.29.24).

Dalvai Ragnoli, M., Singer, G., 2024. The River Runner: a low-cost sensor prototype for continuous dissolved greenhouse gas measurements. Journal of Sensors and Sensor Systems 13 (1), 41–61. https://doi.org/10.5194/jsss-13-41-2024.

Destatis (2021). Landwirtschaftszählung 2020. Atlas Agrarstatistik Deutschland: Anteil der Ökofläche. Statistisches Bundesamt. URL: https://agraratlas.statistikportal.de/.

Destatis, 2024. Bodenfläche (tatsächliche Nutzung). Flächenerhebung nach Art der tatsächlichen Nutzung, Statistisches Bundesamt. URL: https://www.destatis.de/DE/Themen/Branchen-Unternehmen/Landwirtschaft-Forstwirtschaft-Fischerei/Flaechennutzung/_inhalt.html#238438.

Dou, Y., Cosentino, F., Malek, Z., Maiorano, L., Thuiller, W., Verburg, P.H., 2021. A new European land systems representation accounting for landscape characteristics. Landscape Ecology 36, 2215–2234. https://doi.org/10.1007/s10980-021-01227-5.

European Environment Agency (EEA), 2017. High Nature Value (HNV) Farmland. European data data.europa.eu. URL: https://data.europa.eu/data/datasets/dat-145-en?locale=en (accessed 7.29.24).

Gao, B., 1996. NDWI—a normalized difference water index for remote sensing of vegetation liquid water from space. Remote Sens. Environ. 58 (3), 257–266. https://doi.org/10.1016/S0034-4257(96)00067-3.

Gitelson, A.A., Merzlyak, M.N., 1998. Remote sensing of chlorophyll concentration in higher plant leaves. Adv. Space Res. 22 (5), 689–692. https://doi.org/10.1016/S0273-1177(97)01133-2.

Gómez-Gener, L., Rocher-Ros, G., Battin, T., Cohen, M.J., Dalmagro, H.J., Dinsmore, K.J., Drake, T.W., Duvert, C., Enrich-Prast, A., Horgby, Å., Johnson, M.S., Kirk, L., Machado-Silva, F., Marzolf, N.S., McDowell, M.J., McDowell, W.H., Miettinen, H., Ojala, A.K., Peter, H., Sponseller, R.A., 2021. Global carbon dioxide efflux from rivers enhanced by high nocturnal emissions. Nat. Geosci. 14 (5), 289–294. https://doi.org/10.1038/s41561-021-00722-3.

Herreid, A.M., Wymore, A.S., Varner, R.K., Potter, J.D., McDowell, W.H., 2021. Divergent controls on stream greenhouse gas concentrations across a land-use gradient. Ecosystems 24 (6), 1299–1316. https://doi.org/10.1007/s10021-020-00584-7.

Horgby, Å., Boix Canadell, M., Ulseth, A.J., Vennemann, T.W., Battin, T.J., 2019a. High-resolution spatial sampling identifies groundwater as driver of CO2 dynamics in an Alpine stream network. J. Geophys. Res. Biogeosci. 124 (7), 1961–1976. https://doi.org/10.1029/2019JG005047.

Horgby, Å., Segatto, P.L., Bertuzzo, E., Lauerwald, R., Lehner, B., Ulseth, A.J., Vennemann, T.W., Battin, T.J., 2019b. Unexpected large evasion fluxes of carbon dioxide from turbulent streams draining the world's mountains. Nature Communications 10 (1). https://doi.org/10.1038/s41467-019-12905-z.

Hotchkiss, E.R., Hall, R.O., Sponseller, R.A., Butman, D., Klaminder, J., Laudon, H., Rosvall, M., Karlsson, J., 2015. Sources of and processes controlling CO2emissions change with the size of streams and rivers. Nat. Geosci. 8 (9), 696–699. https://doi.org/10.1038/ngeo2507.

Hu, M., Chen, D., Dahlgren, R.A., 2016. Modeling nitrous oxide emission from rivers: a global assessment. Glob. Chang. Biol. 22 (11), 3566–3582. https://doi.org/10.1111/gcb.13351.

Jones, M.W., Peters, G.P., Gasser, T., Andrew, R.M., Schwingshackl, C., Gütschow, J., Houghton, R.A., Friedlingstein, P., Pongratz, J., Le Quéré, C., 2023. National contributions to climate change due to historical emissions of carbon dioxide, methane, and nitrous oxide since 1850. Scientific Data 10 (1). https://doi.org/10.1038/s41597-023-02041-1.

Koschorreck, M., Kamjunke, N., Koedel, U., Rode, M., Schuetze, C., Bussmann, I., 2024. Diurnal versus spatial variability of greenhouse gas emissions from an anthropogenically modified lowland river in Germany. Biogeosciences 21 (6), 1613–1628. https://doi.org/10.5194/bg-21-1613-2024.

Lauerwald, R., Allen, G.H., Deemer, B.R., Liu, S., Maavara, T., Raymond, P., Alcott, L., Bastviken, D., Hastie, A., Holgerson, M.A., Johnson, M.S., Lehner, B., Lin, P., Marzadri, A., Ran, L., Tian, H., Yang, X., Yao, Y., Regnier, P., 2023. Inland water greenhouse gas budgets for RECCAP2: 2. Regionalization and homogenization of estimates. In: Global Biogeochemical Cycles, vol. 37. John Wiley and Sons Inc. https://doi.org/10.1029/2022GB007658. Issue 5.

Leith, F.I., Dinsmore, K.J., Wallin, M.B., Billett, M.F., Heal, K.V., Laudon, H., Öquist, M. G., Bishop, K., 2015. Carbon dioxide transport across the hillslope-riparian-stream continuum in a boreal headwater catchment. Biogeosciences 12 (6), 1881–1902. https://doi.org/10.5194/bg-12-1881-2015.

Leng, P., Kamjunke, N., Li, F., Koschorreck, M., 2021. Temporal patterns of methane emissions from two streams with different riparian connectivity. Journal of Geophysical Research: Biogeosciences 126 (8). https://doi.org/10.1029/2020JG006104.

Li, M., Peng, C., Zhang, K., Xu, L., Wang, J., Yang, Y., Li, P., Liu, Z., He, N., 2021. Headwater stream ecosystem: an important source of greenhouse gases to the atmosphere. Water Res. 190. https://doi.org/10.1016/j.watres.2020.116738.

Liu, S., Kuhn, C., Amatulli, G., Aho, K., Butman, D.E., Allen, G.H., Lin, P., Pan, M., Yamazaki, D., Brinkerhoff, C., Gleason, C., Xia, X., Raymond, P.A., 2022. The Importance of Hydrology in Routing Terrestrial Carbon to the Atmosphere via Global Streams and Rivers. https://doi.org/10.1073/pnas.2106322119/-/DCSupplemental.

Liu, B., Wang, Z., Tian, M., Yang, X., Chan, C.N., Chen, S., Yang, Q., Ran, L., 2023. Basin-scale CO_2 emissions from the East River in South China: importance of small rivers, human impacts and monsoons. Journal of Geophysical Research: Biogeosciences 128 (1). https://doi.org/10.1029/2022JG007291.

Manske, D., Grosch, L., Schmiedt, J., 2022. Geo-locations and System Data of Renewable Energy Installations in Germany. https://doi.org/10.5281/zenodo.6920931.

Martinsen, K.T., Kragh, T., Sand-Jensen, K., 2020. Carbon dioxide partial pressure and emission throughout the Scandinavian stream network. Global Biogeochem. Cycles 34 (12). https://doi.org/10.1029/2020GB006703.

Marzadri, A., Amatulli, G., Tonina, D., Bellin, A., Shen, L.Q., Allen, G.H., Raymond, P.A., 2021. Global riverine nitrous oxide emissions: the role of small streams and large rivers. Sci. Total Environ. 776, 145148. https://doi.org/10.1016/j.scitotenv.2021.145148.

Masese, F.O., Salcedo-Borda, J.S., Gettel, G.M., Irvine, K., McClain, M.E., 2017. Influence of catchment land use and seasonality on dissolved organic matter composition and ecosystem metabolism in headwater streams of a Kenyan river. Biogeochemistry 132 (1–2), 1–22. https://doi.org/10.1007/s10533-016-0269-6.

Michaelis, T., Kaplar, F., Baumann, T., Wunderlich, A., Einsiedl, F., 2024. High methane ebullition throughout one year in a regulated central European stream. Sci. Rep. 14 (1). https://doi.org/10.1038/s41598-024-54760-z.

Mwanake, R., 2023. Water quality and greenhouse gas (GHG) concentration data for temperate headwater streams in Germany. In: Radar 4 KIT. Karlsruhe Institute of Technology (KIT); Karlsruhe Institute of Technology - Institute of Meteorology and Climate Research - Atmospheric Environmental Research (IMK-IFU). https://doi.org/10.35097/1684.

Mwanake, R.M., Gettel, G.M., Aho, K.S., Namwaya, D.W., Masese, F.O., Butterbach-Bahl, K., Raymond, P.A., 2019. Land use, not stream order, controls N2O concentration and flux in the Upper Mara River Basin, Kenya. Journal of Geophysical Research: Biogeosciences 124 (11), 3491–3506. https://doi.org/10.1029/2019JG005063.

Mwanake, R.M., Gettel, G.M., Ishimwe, C., Wangari, E.G., Butterbach-Bahl, K., Kiese, R., 2022. Basin-scale estimates of greenhouse gas emissions from the Mara River, Kenya: importance of discharge, stream size, and land use/land cover. Limnol. Oceanogr. 67 (8), 1776–1793. https://doi.org/10.1002/lno.12166.

Mwanake, R.M., Gettel, G.M., Wangari, E.G., Glaser, C., Houska, T., Breuer, L., Butterbach-Bahl, K., Kiese, R., 2023a. Anthropogenic activities significantly increase annual greenhouse gas (GHG) fluxes from temperate headwater streams in Germany. Biogeosciences 20 (16), 3395–3422. https://doi.org/10.5194/bg-20-3395-2023.

Mwanake, R.M., Gettel, G.M., Wangari, E.G., Butterbach-Bahl, K., Kiese, R., 2023b. Interactive effects of catchment mean water residence time and agricultural area on

water physico-chemical variables and GHG saturations in headwater streams. Frontiers in Water 5. https://doi.org/10.3389/frwa.2023.1220544.
Mwanake, R.M., Imhof, H.K., Kiese, R., 2024. Divergent drivers of the spatial variation in greenhouse gas concentrations and fluxes along the Rhine River and the Mittelland Canal in Germany. Environ. Sci. Pollut. Res. https://doi.org/10.1007/s11356-024-33394-8.
Olsen, A., Triñanes, J.A., Wanninkhof, R., 2004. Sea–air flux of CO2 in the Caribbean Sea estimated using in situ and remote sensing data. Remote Sens. Environ. 89 (3), 309–325. https://doi.org/10.1016/j.rse.2003.10.011.
Panique-Casso, D.G., Goethals, P., Ho, L., 2024. Modeling greenhouse gas emissions from riverine systems: a review. In: Water Research, vol. 250. Elsevier Ltd. https://doi.org/10.1016/j.watres.2023.121012
Parard, G., Charantonis, A.A., Rutgerson, A., 2015. Remote sensing the sea surface CO_2 of the Baltic Sea using the SOMLO methodology. Biogeosciences 12 (11), 3369–3384. https://doi.org/10.5194/bg-12-3369-2015.
Park, J.-H., Lee, H., Zhumabieke, M., Kim, S.-H., Shin, K.-H., Khim, B.-K., 2023. Basin-specific pollution and impoundment effects on greenhouse gas distributions in three rivers and estuaries. Water Res. 236, 119982. https://doi.org/10.1016/j.watres.2023.119982.
Peterse, I.F., Hendriks, L., Weideveld, S.T.J., Smolders, A.J.P., Lamers, L.P.M., Lücker, S., Veraart, A.J., 2024. Wastewater-effluent discharge and incomplete denitrification drive riverine CO_2, CH_4 and N_2O emissions. Sci. Total Environ. 951. https://doi.org/10.1016/j.scitotenv.2024.175797.
Piatka, D.R., Wild, R., Hartmann, J., Kaule, R., Kaule, L., Gilfedder, B., Peiffer, S., Geist, J., Beierkuhnlein, C., Barth, J.A.C., 2021. Transfer and transformations of oxygen in rivers as catchment reflectors of continental landscapes: a review. In: Earth-Science Reviews, vol. 220. Elsevier B.V. https://doi.org/10.1016/j.earscirev.2021.103729.
Piatka, D.R., Nánási, R.L., Mwanake, R.M., Engelsberger, F., Willibald, G., Neidl, F., Kiese, R., 2024. Precipitation fuels dissolved greenhouse gas (CO_2, CH_4, N_2O) dynamics in a peatland-dominated headwater stream: results from a continuous monitoring setup. Frontiers in Water 5. https://doi.org/10.3389/frwa.2023.1321137.
Preidl, S., Lange, M., Doktor, D., 2020. Introducing APiC for regionalised land cover mapping on the national scale using Sentinel-2A imagery. Remote Sensing of Environment 240, 111673. https://doi.org/10.1016/j.rse.2020.111673.
Premke, K., Wurzbacher, C., Felsmann, K., Fabian, J., Taube, R., Bodmer, P., Attermeyer, K., Nitzsche, K.N., Schroer, S., Koschorreck, M., Hübner, E., Mahmoudinejad, T.H., Kyba, C.C.M., Monaghan, M.T., Hölker, F., 2022. Large-scale sampling of the freshwater microbiome suggests pollution-driven ecosystem changes. Environ. Pollut. 308, 119627. https://doi.org/10.1016/j.envpol.2022.119627.
Qi, T., Shen, M., Kutser, T., Xiao, Q., Cao, Z., Ma, J., Luo, J., Liu, D., Duan, H., 2023. Remote sensing of dissolved CO2 concentrations in meso-eutrophic lakes using Sentinel-3 imagery. Remote Sens. Environ. 286, 113431. https://doi.org/10.1016/j.rse.2022.113431.
Quick, A.M., Reeder, W.J., Farrell, T.B., Tonina, D., Feris, K.P., Benner, S.G., 2019. Nitrous oxide from streams and rivers: A review of primary biogeochemical pathways and environmental variables. In: Earth-Science Reviews, vol. 191. Elsevier B.V, pp. 224–262. https://doi.org/10.1016/j.earscirev.2019.02.021.
Raymond, P.A., Zappa, C.J., Butman, D., Bott, T.L., Potter, J., Mulholland, P., Laursen, A. E., McDowell, W.H., Newbold, D., 2012. Scaling the gas transfer velocity and hydraulic geometry in streams and small rivers. Limnology and Oceanography: Fluids and Environments 2 (1), 41–53. https://doi.org/10.1215/21573689-1597669.
Raymond, P.A., Hartmann, J., Lauerwald, R., Sobek, S., McDonald, C., Hoover, M., Butman, D., Striegl, R., Mayorga, E., Humborg, C., Kortelainen, P., Dürr, H., Meybeck, M., Ciais, P., Guth, P., 2013. Global carbon dioxide emissions from inland waters. Nature 503 (7476), 355–359. https://doi.org/10.1038/nature12760.
Rocher-Ros, G., Stanley, E.H., Loken, L.C., Casson, N.J., Raymond, P.A., Liu, S., Amatulli, G., Sponseller, R.A., 2023. Global methane emissions from rivers and streams. Nature. https://doi.org/10.1038/s41586-023-06344-6.
Schade, J.D., Bailio, J., McDowell, W.H., 2016. Greenhouse gas flux from headwater streams in New Hampshire, USA: patterns and drivers. Limnol. Oceanogr. 61, S165–S174. https://doi.org/10.1002/lno.10337.
Stanley, E.H., Casson, N.J., Christel, S.T., Crawford, J.T., Loken, L.C., Oliver, S.K., 2016. The ecology of methane in streams and rivers: patterns, controls, and global significance. In: Ecological Monographs, vol. 86. Ecological Society of America, pp. 146–171. https://doi.org/10.1890/15-1027. Issue 2.
Stanley, E.H., Loken, L.C., Casson, N.J., Oliver, S.K., Sponseller, R.A., Wallin, M.B., Zhang, L., Rocher-Ros, G., 2023. GRiMeDB: the Global River Methane Database of concentrations and fluxes. Earth System Science Data 15 (7), 2879–2926. https://doi.org/10.5194/essd-15-2879-2023.
Upadhyay, P., Prajapati, S.K., Kumar, A., 2023. Impacts of riverine pollution on greenhouse gas emissions: a comprehensive review. Ecol. Indic. 154, 110649. https://doi.org/10.1016/j.ecolind.2023.110649.
Valerio, A.M., Kampel, M., Ward, N.D., Sawakuchi, H.O., Cunha, A.C., Richey, J.E., 2021. CO_2 partial pressure and fluxes in the Amazon River plume using in situ and remote sensing data. Cont. Shelf Res. 215, 104348. https://doi.org/10.1016/j.csr.2021.104348.
Wang, J., Wang, G., Zhang, S., Xin, Y., Jiang, C., Liu, S., He, X., McDowell, W.H., Xia, X., 2022. Indirect nitrous oxide emission factors of fluvial networks can be predicted by dissolved organic carbon and nitrate from local to global scales. Glob. Chang. Biol. 28 (24), 7270–7285. https://doi.org/10.1111/gcb.16458.
Wang, S., Lan, B., Yu, L., Xiao, M., Jiang, L., Qin, Y., Jin, Y., Zhou, Y., Armanbek, G., Ma, J., Wang, M., Jetten, M.S.M., Tian, H., Zhu, G., Zhu, Y.G., 2024. Ammonium-derived nitrous oxide is a global source in streams. Nature Communications 15 (1). https://doi.org/10.1038/s41467-024-48343-9.
Wangari, E.G., Mwangada Mwanake, R., Houska, T., Kraus, D., Gettel, G.M., Kiese, R., Breuer, L., Butterbach-Bahl, K., 2023. Identifying landscape hot and cold spots of soil greenhouse gas fluxes by combining field measurements and remote sensing data. Biogeosciences 20 (24), 5029–5067. https://doi.org/10.5194/bg-20-5029-2023.
Wilkinson, J., Bodmer, P., Lorke, A., 2019. Methane dynamics and thermal response in impoundments of the Rhine River, Germany. Sci. Total Environ. 659, 1045–1057. https://doi.org/10.1016/j.scitotenv.2018.12.424.
Willmott, C., Matsuura, K., 2005. Advantages of the mean absolute error (MAE) over the root mean square error (RMSE) in assessing average model performance. Climate Res. 30, 79–82. https://doi.org/10.3354/cr030079.
Winkler, K., Fuchs, R., Rounsevell, M., Herold, M., 2021. Global land use changes are four times greater than previously estimated. Nature Communications 12, 2501. https://doi.org/10.1038/s41467-021-22702-2.
Woodrow, R.L., White, S.A., Conrad, S.R., Wadnerkar, P.D., Rocher-Ros, G., Sanders, C. J., Holloway, C.J., Santos, I.R., 2024. Enhanced stream greenhouse gas emissions at night and during flood events. In: Limnology And Oceanography Letters. John Wiley and Sons Inc. https://doi.org/10.1002/lol2.10374
Xiong, C., Tao, H., Liu, S., Liu, G., Wen, Z., Shang, Y., Wang, Q., Fang, C., Li, S., Song, K., 2024. Using satellite imagery to estimate CO2 partial pressure and exchange with the atmosphere in the Songhua River. J. Hydrol. 634. https://doi.org/10.1016/j.jhydrol.2024.131074.
Xu, F., Coco, G., Zhou, Z., Townend, I., Guo, L., He, Q., 2020. A universal form of power law relationships for river and stream channels. Geophys. Res. Lett. 47 (20). https://doi.org/10.1029/2020GL090493.
Xu, W., Wang, G., Liu, S., Wang, J., McDowell, W.H., Huang, K., Raymond, P.A., Yang, Z., Xia, X., 2024. Globally elevated greenhouse gas emissions from polluted urban rivers. Nature Sustainability. https://doi.org/10.1038/s41893-024-01358-y.